Prior heterogeneous ice nucleation events shape homogeneous freezing during the evolution of synoptic cirrus

Kasper Juurikkala^{1,2}, Christina J. Williamson^{1,3}, Karl D. Froyd^{4,5}, Jonathan Dean-Day⁶, and Ari Laaksonen^{1,7}

Correspondence: Kasper Juurikkala (kasper.juurikkala@fmi.fi)

Abstract. In situ observations are currently used to classify synoptic cirrus as formed by homogeneous or heterogeneous ice nucleation based on ice residual analysis. We use UCLALES-SALSA to show the limitations of this method by demonstrating that prior heterogeneous freezing events can shape the thermodynamic conditions for homogeneous freezing to occur more likely in subsequent nucleation events.

In a single-cloud case study of synoptic cirrus from NASA's Midlatitude Airborne Cirrus Properties Experiment (MACPEX), observations suggest homogeneous freezing as the dominant nucleation mechanism, despite the other mission days with synoptic cirrus showing generally heterogeneous freezing characteristics. Model simulations reveal that ice residual analysis cannot capture influence of earlier heterogeneous freezing events, where mineral dust acted as ice-nucleating particles (INPs). These earlier events depleted INPs at cloud-forming altitudes, enabling homogeneous freezing at the time of observations. Cirrus cloud properties were simulated using measured meteorological and aerosol conditions and compared with observed cloud structures. Results show that modeling the impact of prior nucleation events on the vertical distribution of mineral dust and humidity in the model is necessary to reproduce the observed cloud characteristics. Heterogeneous freezing played a role in the removal of active mineral dust from cloud-forming altitudes well before arriving at the measurement location, while having limited role in forming ice crystals shortly before the time of measurements.

Simulations also show that small-scale wave activity significantly influenced ice nucleation efficiency and cloud properties. Although large-scale atmospheric dynamics typically dominate synoptic cirrus formation, they alone were insufficient to replicate the observed cloud characteristics.

1 Introduction

The 2021 IPCC report (Forster et al., 2021) highlights that clouds and aerosols remain one of the primary sources of uncertainty in the Earth's energy budget and our ability to predict future climate. The intricate interactions between these atmospheric com-

¹Finnish Meteorological Institute, 00560 Helsinki, Finland

²Department of Physics, University of Helsinki, Helsinki, 00014, Finland

³Institute for Atmospheric and Earth System Research/Physics, University of Helsinki, Helsinki, 00014, Finland

⁴Cooperative Institute for Research in Environmental Sciences, University of Colorado, Boulder, Colorado 80309, USA

⁵Air Innova Research and Consulting, Boulder, CO 80305, USA

⁶Bay Area Environmental Research Institute, Moffett Field, CA 94035, USA

⁷Department of Technical Physics, University of Eastern Finland, 70211 Kuopio, Finland

ponents pose significant challenges for climate modelling, particularly because microphysical processes occur at small spatial scales that cannot be directly resolved in general circulation models (GCMs) (Burrows et al., 2022). As a result, parametrizations are necessary, requiring a delicate balance between simplicity, realism, computational stability, and efficiency (Boucher et al., 2013).

Another substantial source of uncertainty in cloud radiative effects arises from the large knowledge gaps regarding humidity, particularly ice supersaturated regions in the upper troposphere and lower stratosphere (UTLS), where in situ cirrus clouds form. At present, information on the large-scale transport of humidity in the UTLS primarily comes from numerical weather prediction (NWP) models, such as the Integrated Forecasting System (IFS) developed by the European Centre for Medium-Range Weather Forecasts (ECMWF, 2016) and the ICOsahedral Non-hydrostatic model (ICON; Zängl et al., 2015; Seifert and Siewert, 2024), used by the German Weather Service. These NWP models rely heavily on observational data to maintain a realistic representation of atmospheric conditions. However, the scarcity of spatially and temporally resolved observations in the UTLS hinders their ability to accurately predict ice supersaturation (S_i).

Over the past few decades, several a number of key measurement campaigns e.g., Pan et al. (2010, START08,BAMS), Jensen et al. (2013b, Wendisch et al. (2016, ACRIDICON-CHUVA), Jensen et al. (2017, ATTREX,BAMS), Pan et al. (2017, CONSTRAST) have been conducted in the UTLS, which are compiled by Krämer et al. (2016); Krämer et al. (2020) and Ngo et al. (2025). These campaigns have shown that high S_i is more common than predicted by NWPs. Such high S_i levels promote the formation of

UTLS cirrus clouds, which form synoptically in the absence of convection. However, given the uncertainties surrounding S_i , the formation mechanisms and occurrence of these synoptically driven cirrus clouds remain poorly quantified.

Cirrus clouds primarily form through two dominant mechanisms: heterogeneous and homogeneous freezing (Pruppacher and Klett, 1997)

- (Pruppacher and Klett, 1997; Cziczo and Froyd, 2014; Kanji et al., 2017). Heterogeneous ice nucleation occurs either via immersion freezing, where insoluble particles —commonly referred to as ice-nucleating particles (INPs) —are embedded in aqueous droplets and trigger freezing, or via deposition nucleation, where water vapor directly deposits onto dry, insoluble particles and freezes. For immersion freezing to occur, the INPs have to be somewhat hydrophilic or acquire a water-soluble coating during atmospheric transport. Electron microscopy studies (e.g., Kojima et al., 2006; Cziczo et al., 2013; Twohy, 2014) of cirrus crystal residuals have found that a substantial fraction of these particles consist of uncoated mineral dust. As coatings on mineral dust tend to suppress their heterogeneous ice nucleation efficiency (shifting the nucleation threshold toward higher supersaturation), deposition nucleation is likely the prevailing formation mechanism in many cases. In contrast, homogeneous freezing occurs in the absence of INPs and takes place when aqueous solution droplets freeze at temperatures below the -38°C
- Ice nucleation in cirrus clouds is shaped by the abundance of ice-nucleating particles (INPs), which govern the efficiency with which heterogeneous ice nucleation suppresses homogeneous freezing. In heterogeneous nucleation, INPs trigger ice formation and are subsequently removed from higher altitudes as ice crystals sediment, whereas homogeneous freezing, occurring without INPs, produces ice crystal concentrations that vary with environmental factors such as temperature and vertical velocity (Kärcher and Lohmann, 2002). Modeling studies have significantly advanced our grasp of these processes (e.g. Sassen and Benson, 2000; Kärcher and Lohmann, 2002; Spichtinger and Cziczo, 2010; Rolf et al., 2012; Krämer et al., 2016; Kärcher et al.,

threshold for pure water and at high S_i (e.g., Schneider et al., 2021; Koop et al., 2000).

2019, 2022) with efforts spanning a range of scales, from high-resolution Large Eddy Simulations (Sölch and Kärcher, 2010) to global models (Liu et al., 2012; Tully et al., 2022; Beer et al., 2024). Yet, despite these advances, accurately representing INPs remains challenging due to their scarcity (0.01 to $100 L^{-1}$ at -30° C; DeMott et al. (2010)) and a lack of good aerosol-aware freezing parameterizations, underscoring the need for refined parameterizations and robust observational constraints (Burrows et al., 2022).

One key method for determining whether a cirrus cloud formed through heterogeneous or homogeneous freezing is ice residual analysis. This technique involves evaporating ice crystals collected from cirrus clouds and analyzing the residual particles to infer the presence and nature of INPs that may have initiated freezing (Froyd et al., 2019). Studies like Cziczo et al. (2013) have used this approach to identify mineral dust and other particles in cirrus residuals, providing valuable clues about the nucleation process. However, while ice residual analysis offers insights into the particles involved, it cannot fully capture the dynamic processes—such as the competition between heterogeneous and homogeneous freezing or the influence of vertical velocity and temperature fluctuations—that led to the observed cloud state. This limitation highlights the need for complementary approaches that can simulate these processes in greater detail.

Large-eddy simulation (LES) models, such as UCLALES-SALSA (Tonttila et al., 2017), provide a powerful tool to address this gap by resolving small-scale turbulence and microphysical interactions at resolutions down to tens of meters, capturing INP-driven processes that coarser models heavily parametrize. This capability is crucial for understanding the complexity of cirrus formation beyond what ice residual analysis can reveal. This work focuses on a single case (part of a multi day campaign) of cirrus observed during the Midlatitude Cirrus Properties Experiment MACPEX campaign (Jensen et al., 2013b), which predominantly exhibited homogeneous freezing among the analysed ice crystals (Cziczo et al., 2013). This raises a key question: why did this particular cirrus cloud form primarily through homogeneous freezing?

2 Methods

2.1 MACPEX campaign

The MACPEX campaign conducted by NASA was an aircraft measurement campaign aimed at investigating cirrus cloud properties (Jensen et al., 2013b). The campaign took place between March and April 2011, involving multiple science flights with the NASA WB-57F science aircraft over the southern United States. A total of 14 science flights were conducted, focusing on synoptic and anvil cirrus clouds, resulting in over 18.5 hours of cirrus sampling. In addition to in situ measurements, remotesensing observations were coordinated to target cirrus clouds along the flight paths.

2.2 Description of the instruments used in the analysis

Ice number concentration, size distribution, and ice water content (IWC) were measured using a number of in situ instruments.

The Two-Dimensional Stereo (2D-S) probe (Lawson et al., 2006) captures shadow images of ice particles using orthogonal laser beams and photodiode arrays. It detects particles from 10 μ m to over 1 mm in diameter, making it suitable for characterizing

ice crystals in cirrus clouds. Due to known overestimations in the smallest size bin $(5-15 \mu m)$, these data were excluded from the analysis (e.g. Jensen et al., 2013b; Krämer et al., 2016). The 2D-S also includes filtering techniques to mitigate crystal shattering artifacts (Lawson, 2011). While the 2D-S can estimate IWC, its limitations, particularly with smaller particles can affect the accuracy of those estimates.

For more precise measurements of ice water content (IWC), we use data from the University of Colorado closed-path tunable diode laser hygrometer (CLH) (Davis et al., 2007). The instrument measures enhanced total water by collecting both water vapor and sublimated ice particles via a subisokinetic inlet. Ice particles are evaporated in a heated absorption cell, and the resulting water vapor is quantified using a tunable diode laser. IWC is then derived by subtracting ambient water vapor and combining with meteorological data such as temperature and pressure. Meteorological parameters, including temperature, pressure, wind, and aircraft motion, were obtained from the Meteorological Measurement System (MMS) (Scott et al., 1990). MMS vertical velocity measurements were filtered to isolate fluctuations relevant to model-scale and mesoscale dynamics using 20 and 150 second running means. Only data from constant-altitude flight legs with vertical aircraft speeds below ± 1 m s⁻¹ were used in the vertical wind analysis. Humidity was measured by several instruments; in this study, the Harvard Water Vapor (HWV) instrument was used. Combined with MMS temperature, HWV data enables calculation of supersaturation over ice (S_i), a key indicator of ice nucleation conditions.

100

105

The NOAA Particle Analysis by Laser Mass Spectrometr instrument (PALMS; Thomson et al., 2000; Froyd et al., 2019) provides real-time, size-resolved chemical composition of aerosol particles in the 0.15– $5~\mu m$ range. Combined with data from the Focused Cavity Aerosol Spectrometer (FCAS II; Jonsson et al., 1995) which provides aerosol measurements from size range of 0.07 to 1.5 μm , the PALMS instrument enables classification of aerosol types and determination of particle-type-resolved number distributions (Froyd et al., 2019), providing both information of in-cloud (ice residual particles) and clear-air aerosol properties. These measurements are crucial for assessing the abundance and chemical composition of INPs relevant for cirrus cloud formation.

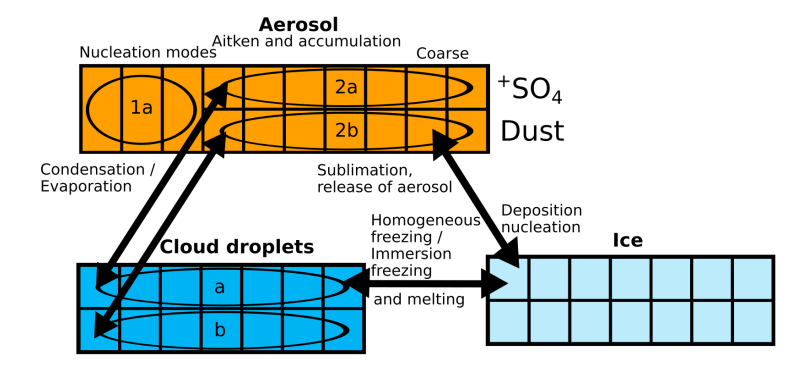


Figure 1. Bin scheme used in UCLALES-SALSA to track particle types relevant to ice nucleation in synoptic cirrus clouds. Freezing of rain is also possible while it is not shown here as it generally does not occur within the realms of this study.

2.3 UCLALES-SALSA

125

130

135

140

UCLALES-SALSA (Tonttila et al., 2017) is a large eddy (LES) model with a combination of sectional aerosol bin microphysics model SALSA (Sectional Aerosol module for Large-Scale Applications) (Kokkola et al., 2008; Tonttila et al., 2017; Kokkola et al., 2018). UCLALES is a well known atmospheric LES model based on the work of Stevens et al. (1999, 2005). The SALSA module enables tracking of four types of particles (including aerosols, cloud droplets, rain/drizzle particles and ice), and their particle size and chemical composition in a bin scheme, shown in Fig. 1. The aerosols are categorized into two distinct bins: one range, from 1a to 2a, addresses particles ranging from nucleation to coarse modes (3 nm – 10 μm), while the other, bin 2b, encompasses sizes above the Aitken and accumulation mode (50 nm – 10 μm). Particles falling within subrange 1a (3 – 50 nm) typically originate from new particle formation (e.g., sulfates) and may include some primary organic particles (Kokkola et al., 2008). This binning strategy enables separate tracking of two aerosol populations with an example: 2a for soluble sulfates crucial in cloud activation, and 2b for mineral dust particles relevant to ice nucleation. Furthermore, this parallel tracking extends to cloud bins, facilitating comparison between the evolution of these two aerosol populations.

Ahola et al. (2020) implemented various freezing mechanisms, however, in this study, mainly homogeneous freezing and deposition nucleation are turned on as the typical temperatures within upper tropospheric cirrus clouds are below -38 $^{\circ}$ C where pure water does not stay in liquid state. By default, UCLALES-SALSA uses homogeneous and heterogeneous ice nucleation parametrization schemes based on Khvorostyanov and Curry (2000), however, due to the heterogeneous ice nucleation schemes being stochastic (time dependent), it was concluded that ice nucleation could be greatly over-estimated in this particular study. To overcome this issue, a deterministic, time-independent deposition nucleation parametrization developed by Ullrich et al. (2017) for uncoated mineral dust particles was implemented to SALSA. This parametrization was created by using a fit to ice nucleation activity of several mineral dust particles presented in Kanji et al. (2011). For this scheme, tracking of activated INP fractions is necessary since deterministic parametrizations base their ice nucleation activity on original INP population. Homogeneous freezing is implemented based on the temperature and S_i relation presented in (Koop et al., 2000).

Once ice nucleation occurs, ice crystals are transferred from aerosol bins to ice bins, where their subsequent evolution is governed by microphysical processes such as vapor deposition, sublimation, and sedimentation. The growth and evaporation of ice crystals are calculated using the framework from Jacobson (2005). Ice sedimentation is explicitly resolved based on size-dependent terminal velocities. Additionally, ice-ice collisions are aggregation, influencing the size distribution of ice crystals over time. To represent ice crystal size distributions, the ice bins in SALSA range from 2 μ m to 400 microns in diameter, ensuring a comprehensive resolution of both small ice crystals and larger particles. Ice crystals below 40 μ m are assumed to be spherical, while those above this threshold are treated as bullet rosettes, following the habit-dependent parameterization in Baum et al. (2005). The habit transition is consistent with in situ cirrus observations that show a prevalence of bullet rosettes in larger particle size ranges. The ability to track the evolution of ice particle sizes is crucial in simulations of cirrus clouds, where the competition between heterogeneous and homogeneous freezing determines cloud properties. The sectional approach in SALSA allows for an accurate representation of ice nucleation pathways, growth dynamics, and size-dependent sedimentation, which are essential for understanding cirrus cloud evolution.

3 Case study-16 April 2011

150

155

A mission flight with the NASA WB-57F was flown on 16th of April to target cirrus cloud trail flowing easterly. The plane took off at 1700 UTC from Houston, Texas, and flew directly towards the cirrus clouds. Before flying into the cirrus clouds, lower stratospheric air was sampled and also provided the meteorological conditions over the cirrus cloud layers. The sampling of cirrus was done by flying back and forth following the cirrus cloud trail. The flight path is presented in Fig. 2.

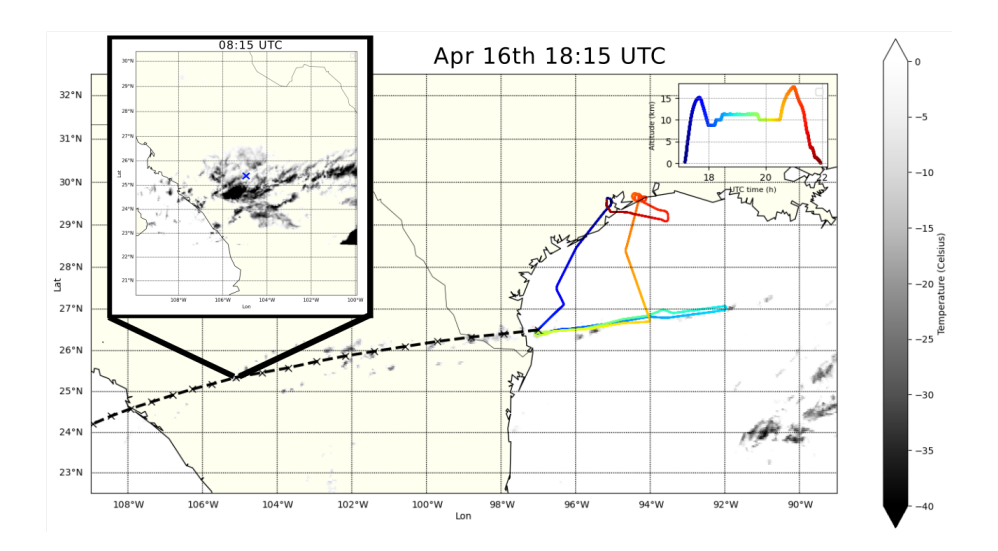


Figure 2. GOES-16 satellite imagery shows infrared radiation (IR) temperature of cirrus cloud tops for 8.15 UTC (top-left focused panel) and 18.15 UTC (base). A back-trace trajectory trajectory with black dashed line and cross marking at every hour is shown, starting from the aircraft's intersection with the cirrus clouds at 18 UTC. The 8.15 UTC imagery with effective cloud-top temperatures below -40°C indicates intense cirrus clouds. A blue cross is marked in the centre of this panel to indicate where the air parcel was located around 8 UTC in the back-trace trajectory. The flight path of the WB-57F on April 16th, 2011, is overlaid with coloured lines representing the aircraft's position. The colour of the flight path corresponds to altitude and time in UTC.

According to ECMWF ERA5 reanalysis (Hersbach, 2023) data, these cirrus clouds formed in a moisture rich layer (10-12 km) originating from the Pacific Ocean, carried by a subtropical jet.

Based on measurements from the Geostationary Operational Environmental Satellite-16 (GOES-16), operated by the National Oceanic and Atmospheric Administration (NOAA), correlated to the location of the WB-57F aircraft, where 2 km thick cirrus cloud layers between 10 and 12 km along the flight path were identified. Figure 3 presents the vertical profile of meteorological variables during aircraft ascents and descents in the proximity of cirrus clouds. As the satellite retrieval suggests, the direct measurements show a layer of cirrus clouds with presence of high supersaturation over ice (S_i) between 10 and 12.5 km. This layer is called as supersaturated layer from now on. The vertical layer where the cirrus clouds are present is stable throughout as the potential temperature gradient is significantly above 0 ($\frac{d\theta}{dz} > 0$). This implies that the formation of these cirrus clouds is

influenced by large-scale forcing, classifying them as synoptic cirrus clouds (e.g. Jensen et al., 2013b). The measured humidity inside the supersaturated layer varies significantly, indicating that vertical wind fluctuations might have a large influence on the humidity inside the cloud. Also, the ECMWF ERA5 reanalysis shows a significant spread in values for S_i along the WB-57F flight path. The S_i in the ERA5 is an average over a grid box of approximately 28×28 km, meaning that a significant portion of variability is lost, while the overall levels of S_i is the same.

160

165

The formation mechanism of cirrus clouds is investigated through back-trajectory calculations conducted with Lagrangian analysis python script, utilizing wind field data from ERA5. As illustrated in Fig. 4, air parcels originating at 10 km appear to undergo major uplift around 4–7 UTC, influenced by topography interacting with the prevailing air-mass over the Western parts of Mexico with mountainous terrain. This uplifting is connected to the rapid development of high ice water content cirrus clouds, as evidenced by cold cloud temperatures in satellite imagery in the region as shown in Fig. 2. The presence of

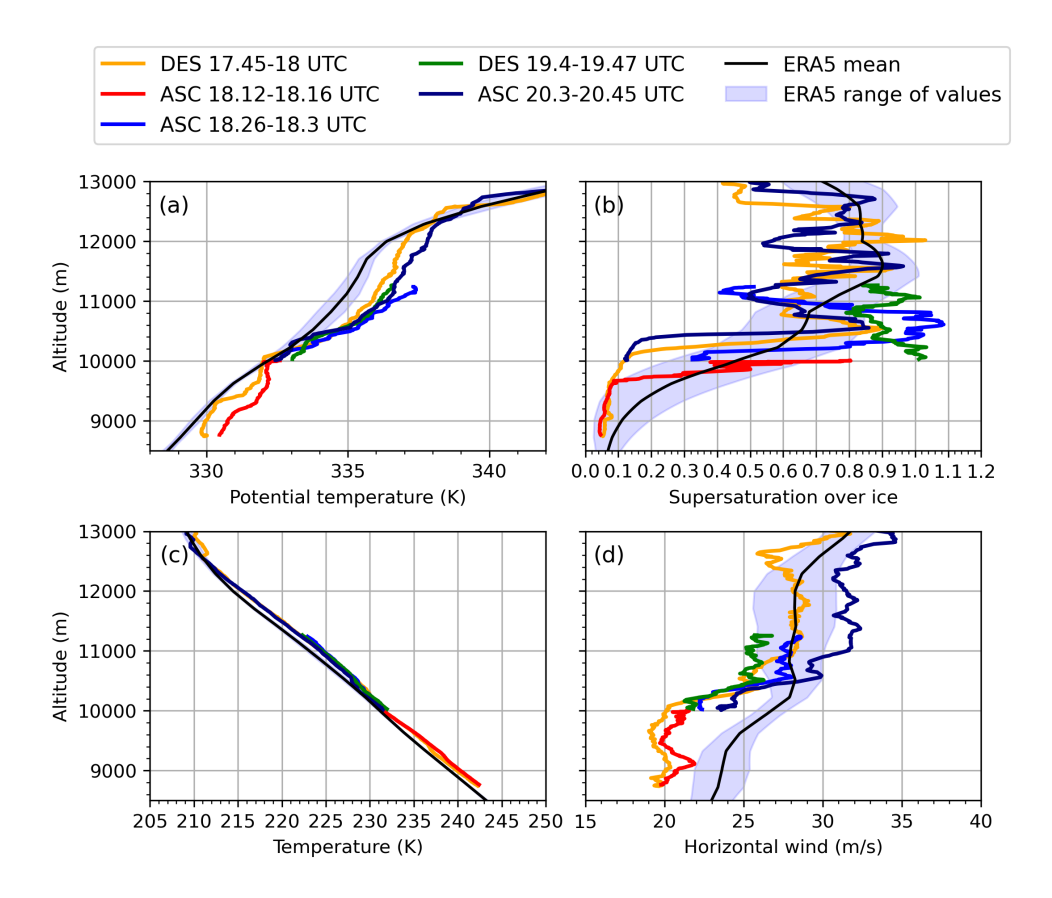


Figure 3. (a) Potential temperature, (b) temperature, (c) supersaturation over ice and (d) horizontal wind measured with MMS during the ascents and descents of the aircraft. The vertical profiles are result of multiple ascents (ASC) and descent (DES) through the cirrus cloud altutudes. ECMWF ERA5 data is shown with shading of light blue representing the $1-\sigma$ around the mean of altitude. Both MMS and 2DS observations are 1Hz data.

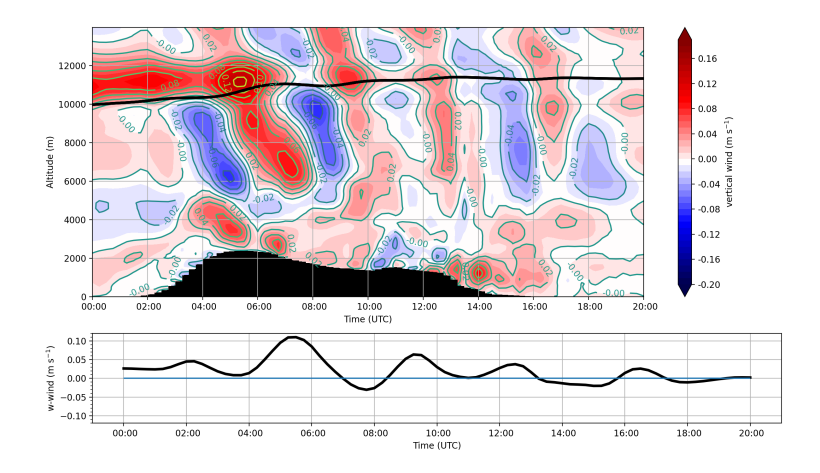


Figure 4. Vertical profile of vertical wind along the back-trajectory analysis moving along the cirrus layer. Black line shows the movement of air parcel starting at 10 km at 0 UTC. The surface elevation directly below the trajectory is in black. The vertical wind around the air-parcel is shown in the lower panel.

mountain ranges induces gravity waves (Smith, 1979; Jensen et al., 1998; Joos et al., 2008, 2009), generating local ascending and descending air patterns downstream from the point of disturbance, even present during the time of WB-57F measurements over the ocean (between 18–20.5 UTC in Fig.4). The data shown strongly suggests that the cirrus cloud formation was induced by these gravity waves with periods of couple hours.

3.1 Indication of homogeneous freezing

170

175

180

185

The April 16th cirrus case was the only observed instance during the MACPEX campaign where the primary nucleation mechanism was predominantly homogeneous freezing (Cziczo et al., 2013). This conclusion is supported by examining the ice residual particle (IRP) populations (Fig. 5). Particles composed of a mix of sulfates, organics, nitrates, and biomass burning particles contain a substantial fraction of water-soluble compounds (Reid et al., 2005), which promote homogeneous nucleation at temperatures below 235 K (Koop et al., 2000). In contrast, high IRP fractions of mineral dust and metallic particles are generally indicative of heterogeneous nucleation (Cziczo et al., 2013). Observations from April 16th revealed substantial fractions of sulfate/organic/nitrate particles (38%) and biomass burning particles (39%) in the IRP, with a much lower fraction of mineral dust (10%) compared to heterogeneously nucleated cirrus cases presented by Cziczo et al. (2013) (see their Fig. 6). Interestingly, mineral dust fractions were higher in the observed IRP compared to clear-air aerosol fractions (Fig. 5), suggesting limited influence of mineral dust on the ice crystal population. This indicates that at least some ice likely formed heterogeneously, albeit not predominantly.

Cziczo et al. (2013) noted that mineral dust and metallic particles, when acting as heterogeneous INPs in cirrus clouds, are typically thinly coated, making them effective for deposition nucleation. However, PALMS spectral analysis showed that sulfate coatings on April 16th were thicker than on other MACPEX flight days (analysis results available in the supplementary

material). Although the data quality is limited, this suggests that well-aged UTLS air results in thicker coatings on mineral dust particles, which may suppress their heterogeneous ice nucleation ability, as has been shown in previous studies (e.g., Cziczo et al., 2009; Eastwood et al., 2009; Chernoff and Bertram, 2010; Sullivan et al., 2010).

PALMS measurements also included uncharacterized particles labeled as "other", which did not have obvious characteristics

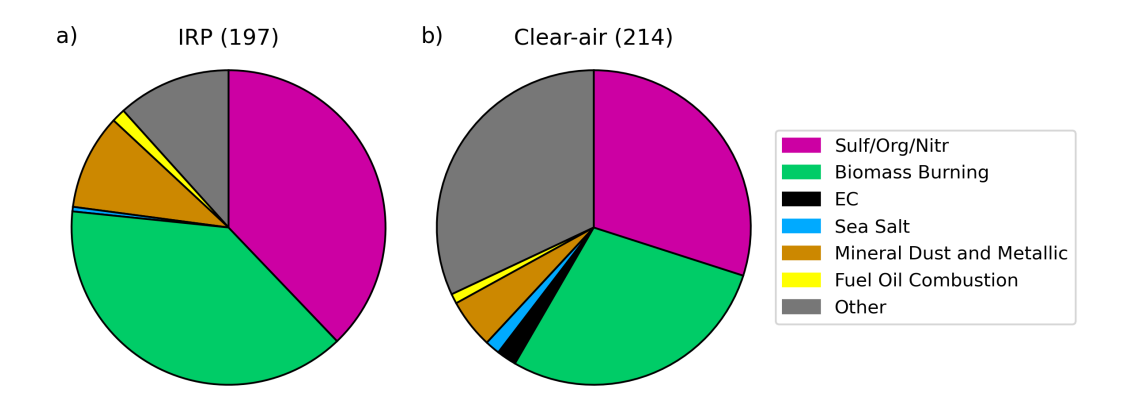


Figure 5. (a) Ice cloud residual and (b) clear-air contribution of aerosol species in a range from 0.2 to 3μ m for IRP and 0.2 to 1.5μ m for clear air.

190

195

200

205

of heterogeneous INP. These accounted for approximately one-third of the clear-air aerosol population, a greater proportion than observed during other MACPEX flights. These particles were compositionally typical of the region, with carbon-rich spectra inconsistent with sulfate/organic mixtures, and included some with pyridinium signatures.

There are some limitations to the analysis of IRP and clear-air particle compositions in this study. By definition, the measured clear-air aerosols are those that did not nucleate into ice at the time of measurement. Alternatively, these aerosols may have been involved in ice nucleation events and subsequent cloud sublimation well before the measurements were taken. Consequently, it is unclear whether these aerosols exhibit the same ice nucleation properties as those measured inside the cloud (IRP). Furthermore, the mineral dust particle fractions are averaged from a very limited clear-air sample set, making direct comparisons with IRP challenging. Additionally, the IRP data is inherently biased toward smaller ice crystals, which could potentially skew the results toward higher fractions of homogeneous IRP. However, clear-air particle fractions on Apr 16 were similar to the regional MACPEX averages.

The clear-air measured mineral dust concentration on April 16th in the upper troposphere (with lower stratospheric air filtration) was 2.05×10^{-2} cm⁻³. These values are slightly lower than the MACPEX campaign average (3.36×10^{-2} cm⁻³), however, in line with expected range of values in low latitude Northern hemisphere measured during ATom campaigns presented in Froyd et al. (2022).

In Fig. 6a, the measured N_i despite the absence of measurements below 15 μ m exceeds the concentration of mineral dust particles or other potential heterogeneous INPs, providing strong evidence that homogeneous freezing played a significant role in shaping the N_i distribution. Homogeneous freezing typically requires S_i levels within the range of 1.46–1.54 at temperatures between 210 and 230 K (calculated with Eq. 10 in Ren and Mackenzie (2005)). The measured S_i in Fig. 6b reveals a notable absence of S_i values above 1.2, however, the measurements mostly represent either environment in the absence of clouds or inside matured cirrus clouds where the high S_i would be difficult to find. Observing high S_i required for homogeneous freezing is inherently challenging, especially within fully developed cirrus clouds, as the available humidity rapidly decreases following a homogeneous freezing event. This reduction is driven by nucleated ice crystals and sedimenting ice crystals from higher altitudes, which deplete the water vapor within the layer. Numerical studies (e.g., Spichtinger and Cziczo, 2010) and in situ measurements (e.g., Jensen et al., 2013a) consistently show that S_i quickly returns to near-equilibrium levels after homogeneous freezing occurs, making it unlikely to detect significantly elevated S_i in measurements. Nevertheless, the high levels of ice water content (IWC) observed within the cirrus clouds (Fig. 6c), occasionally coinciding with elevated S_i values—indicative of recent homogeneous freezing events (see supplementary Fig. S5)—support the hypothesis that these cirrus clouds most likely formed via homogeneous freezing (Krämer et al., 2016). Additionally, the median N_i is high and IWC low in the upper levels of cirrus, suggesting that the ice nucleation has occurred substantially in the upper parts of the supersaturated layer. The lack of high S_i in the lower parts of cirrus at 10 km can be explained by the large quantity of water vapor deposited on the sedimenting ice crystals.

Finally, the vertical winds measured within the cirrus were of significantly higher magnitude than those typically associated with synoptic-scale motions, as shown in Fig.7. This suggests that S_i may have experienced considerable short-timescale variability, enabling the threshold for homogeneous freezing to be reached through strong upward motions. Figure 7 presents the frequency distributions of observed vertical wind velocities during constant-altitude flight legs, with the vertical motions caused by aircraft ascents and descents and short scale systematic error filtered out.

3.2 Model setup

215

220

225

235

The UCLALES-SALSA simulations aim to attain results that closely align with measured data. The troposphere from the surface (0 km) to 14 km is simulated using a 3D domain to explore the impact of horizontal variability. The vertical resolution is set to $\Delta z = 300$ m below 6 km and $\Delta z = 50$ m above 7 km. Above 12,5 km, the vertical resolution is lowered linearly to $\Delta z = 300$ m. The resolution is linearly decreased between 6 and 7 km. The vertical grid points are initialized by reading from file zm_grid_in. The time step is capped at a maximum of $\Delta t = 1$ s, which is suitable for simulating cloud microphysics. Data output is recorded at intervals of 5 minutes. The domain size spans 3×3 km with a horizontal resolution of $\Delta x = \Delta y = 50$ m in each direction. This resolution enables the simulation of small-scale eddies (Bryan et al., 2003). Additionally, sensitive tests are done by switching off ice nucleation processes and radiation scheme, and also running a 1D column simulations to examine horizontal variability free conditions. The meteorological variables used for the initial profile come from combined products of WB-57F measurements during the first descend towards the cirrus cloud layers before 18 UTC and the ERA5, shown in Fig. 8. The measurements made during this descend provides information from meteorological conditions throughout the cirrus clouds

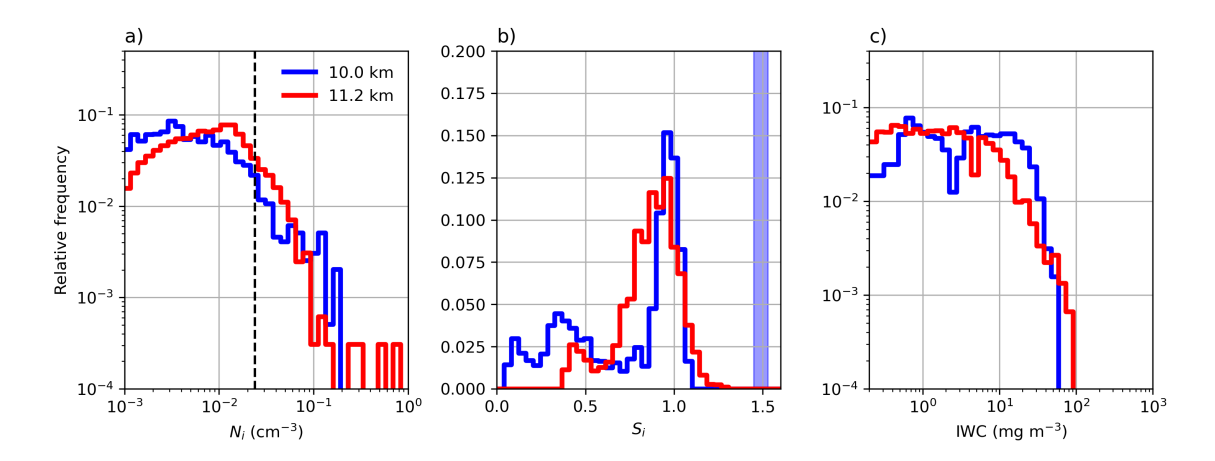


Figure 6. (a) Distribution of N_i measured with 2DS inside cirrus clouds at two constant altitude levels with most continuous time series measured. Dashed line is drawn at the concentration of the mean clear-air concentration of mineral dust $(2.05 \times 10^{-2} \text{ cm}^{-3})$ by PALMS-FCAS (b) Supersaturation over ice (S_i) measured at two constant altitude levels with HWV-MMS. Blue shading indicates homogeneous freezing threshold S_i between 210–230 K based on equation presented in (Ren and Mackenzie, 2005). (c) Ice water content (IWC) is from CLH measurements.

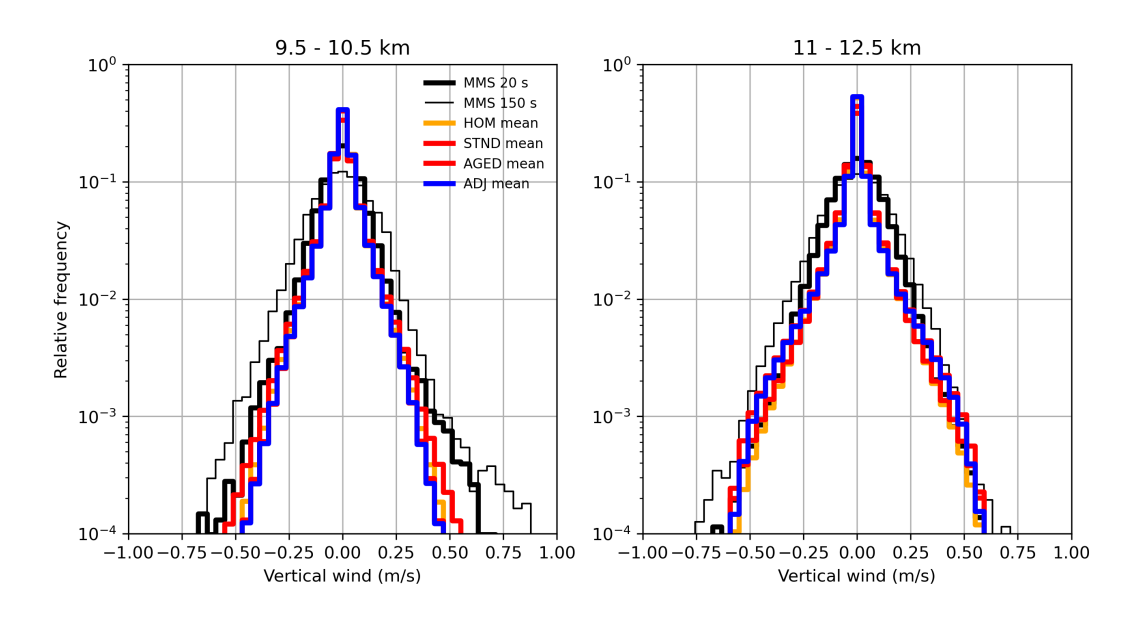


Figure 7. Frequency distribution of vertical wind in two altitudes for the MMS measured continuous statistical data with 20 and 150 second running mean filtering (black lines) and model data for all of the simulation set ups in (colored lines). The left panel represents a constant flight legs at altitude 10.0 km and the right panel at 11.2 km.

altitudes from 9 to 15 km. Data from ERA5 is used for the profile below 9 km as the aircraft did not descend below that altitude. It is, however, concluded that the lower resolution of the ERA5 is sufficient for lower altitudes as the dynamical effects of lower

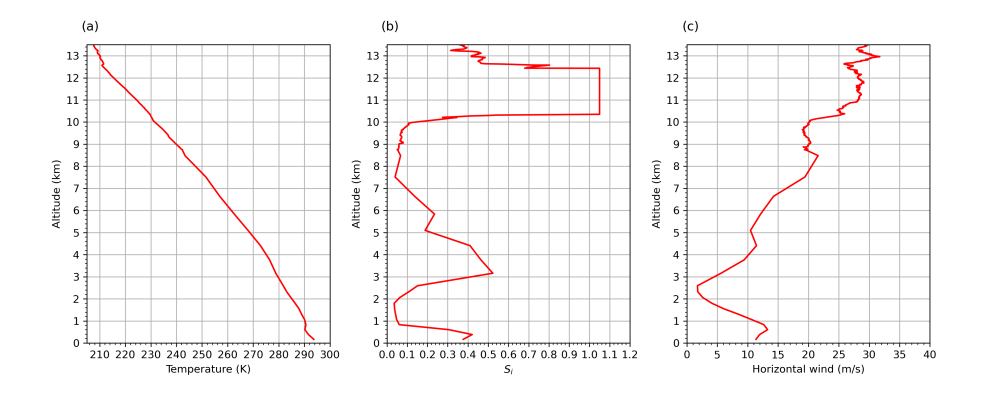


Figure 8. Initial profiles of (a) temperature, (b) supersaturation over ice and (c) horizontal wind used in the simulations.

250

255

atmosphere has limited effect on the cirrus cloud layer as the atmosphere is relatively stable throughout. The stability within the supersaturated layer was relatively high and convection can not be expected. The temperature and humidity fields are perturbed with standard deviations of approximately $\sigma_{\theta} = 0.025$ K and $\sigma_{q} = 2 \cdot 10^{-6}$ kg kg⁻¹. These values are in the same order of magnitude to the values measured with WB-57F inside high humidity layers. The initial S_{i} in the supersaturated layer between levels of 10 and 12.1 km is set to $S_{i} = 1.05$, approximately corresponding to the equilibrium humidity levels typically observed in fully matured cirrus clouds. Satellite imagery revealed that new cirrus clouds tended to form or intensify predominantly in regions where existing cirrus clouds were already present. To simulate the effects of large-scale forcing observed in backtrajectory analysis, a constant updraught is applied to the model domain. Constant updraught values of $w_{\rm LS} = 2,3,4,5$ cm s⁻¹ is used to simulate the effects of varying magnitude on the ice nucleation. After the model domain is lifted by 300 m, the ascent motion is halted. The 300 m lift corresponds to approximate maximum perturbation observed in the back-trajectory analysis. The lifting of the air leads to cooling rates given by the following formulation:

$$\frac{dT}{dt} = \frac{dT}{dz}\frac{dz}{dt} = -\frac{g}{c_p}w_{LS} = -\Gamma \cdot w_{LS} \tag{1}$$

where Γ denotes the dry lapse rate (K km⁻¹), g and c_p denote the gravitational acceleration and the specific heat capacity for constant pressure. The cooling in turn increases the S_i as colder air has lower capacity to hold humidity. The initial choice of S_i significantly influences how high S_i can rise during a limited updraught duration. For instance, with a lapse rate of $\Gamma=10$ K km⁻¹, the maximum cooling achieved with 300 m of lift corresponds to a temperature decrease of approximately 3 K. This, in turn, leads to an estimated increase in supersaturation of $\Delta S_i \approx 0.45$. The S_i levels after 300 m of lift correspond to level required for homogeneous freezing.

Additionally, the model domain experiences horizontal fluctuations in temperature, humidity and wind, and thus they are sensitive to more than the large scale forcing alone. For that, sensitivity runs are done without large scale forcing, radiation scheme and ice nucleation. Each simulation has 4 hour spin-up period where cloud microphysics and large scale forcing are disabled. The length of the spin-up was decided based on the relaxation of turbulent kinetic energy around 4 hours into the simulations. In this case study, mineral dust is treated as the only insoluble aerosol particle or heterogeneous INP, while other insoluble

aerosols were possibly present in aerosol population such as soot from biomass burning were excluded from heterogeneous INP population. The UCLALES-SALSA is run with two different concentrations of mineral dust: at the measured concentration (2.05×10⁻² cm⁻³) and at a reduced concentration, corresponding to 0.1 of the measured concentration (presented in Table 2). The reduced concentration represents a case where the mineral dust has lower INP activity due to coating, or has been scavenged by previous cirrus formation events. These runs are referred to as STND (standard) and AGED respectively from hereafter.

275

280

285

On the other hand, the rest of the observed aerosols (sulfate/organic/nitrate, biomass burning and other particles) are treated as soluble sulfate particles (H₂SO₄) and they are allocated to a-bins which potentially nucleate via homogeneous freezing from aqueous soluble droplets. The concentration of sulfates is set at constant 34.9 cm⁻³ based on the FCAS mission average total concentration. The aerosols of both a- and b-bins are distributed into four modes of log normal distributions and the parameters are shown in Table 1. Other possible insoluble aerosol such as black carbon are not included in the simulations. Notice that most of the soluble aerosols acting in homogeneous freezing are not measured by PALMS-FCAS due to the residual analysis restricted to aerosols above 0.2 µm. The FCAS concentration (total aerosol) includes a large number of aerosols most likely acting as cloud condensation nuclei required for homogeneous freezing but also a small but insignificant fraction of heterogeneous INPs. Also the homogeneous freezing is known to be mostly. Homogeneous freezing has often been described as largely insensitive to the concentration or size distribution of available aerosols unless the concentration is very low (Kärcher and Lohmann, 2002; Jensen et al., 2010) and thus the use of campaign average of soluble aerosols is justifiable. (Kärcher and Lohmann, 2002; Jensen et al., 2010). However, more recent studies (Baumgartner et al., 2022) indicate that under certain conditions, particularly at very cold temperatures and high updraft velocities, the aerosol size distribution can influence freezing. This choice for using the campaign-averaged concentration and size distribution is justified because the resulting number of solution droplets available for homogeneous freezing remains substantially higher than the concentration of heterogeneous INPs, such that homogeneous freezing still produces higher ice concentrations. Our analysis therefore focuses on how heterogeneous ice nucleation shapes the evolution of S_i , while also comparing the relative contributions from homogeneous versus heterogeneous ice nucleation.

	$D_{g,1}$	σ_1	$N_{t,1}$	$D_{g,2}$	σ_2	$N_{t,2}$	$D_{g,3}$	σ_3	$N_{t,3}$	$D_{g,4}$	σ_4	$N_{t,4}$
Sulfates	0.118	1.19	27.3	0.183	1.3	5.76	0.444	1.29	0.049	0.722	1.13	0.010
Mineral dust	0.207	1.3	0.0178	0.222	1.04	0.363	0.476	1.09	0.0033	0.737	1.13	0.0003

Table 1. Parameters of the four log normal distributions. Geometric mean diameter D_g , geometric standard deviation σ and mode total number concentration N_t in cm⁻³.

Setup	Dust profile	Ice nucleation mechanisms	Humidity profile		
STND	const. $2.05 \times 10^{-2} \text{ cm}^{-3}$	het and hom	$S_i = 1.05$		
AGED	const. $2.05 \times 10^{-3} \text{ cm}^{-3}$	het and hom	$S_i = 1.05$		
ADJ	adjusted profile	het and hom	adjusted profile		
НОМ	adjusted profile	hom	adjusted profile		

Table 2. Dust profile, ice nucleation mechanisms and humidity profile used in model run setups. Information regarding adjusted setups ADJ and HOM are explained in Sect. 4.3.

4 Comparison of simulation data to observations

290 4.1 The effect of aged mineral dust on ice nucleation activity

In the STND runs (Fig. 9, upper panels), the combination of heterogeneous ice nucleation and vapor deposition growth of ice crystals effectively suppresses the increase in S_i , preventing it from reaching levels required for homogeneous freezing. Even with an updraft of $w_{\rm LS} = 5~{\rm cm~s^{-1}}$ (Fig. 9d), where growing ice crystals have less time to consume water vapor, the suppression remains strong enough to inhibit homogeneous freezing. This indicates that the measured mineral dust concen-

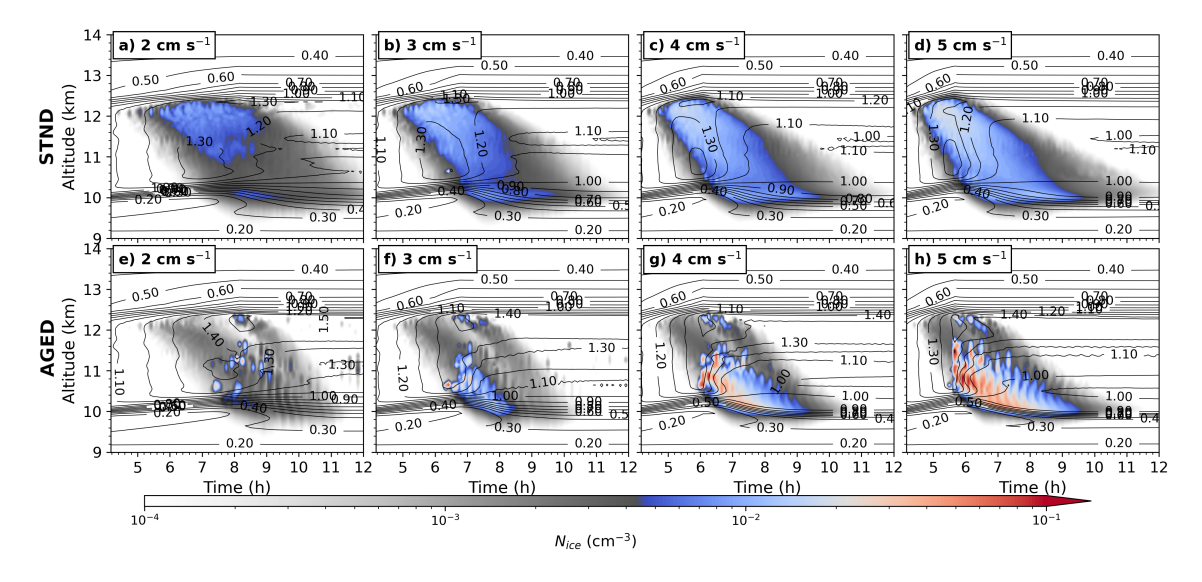


Figure 9. Cirrus clouds simulated with $w_{LS} = 2 - 5$ cm s⁻¹ for measured mineral dust concentrations (STND; a-d) and reduced mineral dust concentrations (AGED; e-h). Black contour lines represent S_i at 0.1 intervals. The color map highlights N_i at critical concentration levels relevant to this study: blue shades correspond to values typically associated with heterogeneous ice nucleation, while red shades indicate concentrations consistent with homogeneous freezing. Grey shades separate blue values from red, as the analysis focuses on high N_i levels in blue and red ranges. The profiles show a 1D vertical slice at the edge of the model domain, with S_i contours representing horizontal averages to reduce noise from horizontal fluctuations.

tration is sufficiently high to prevent competition between homogeneous and heterogeneous ice nucleation mechanisms. If the constant updraft had persisted longer, homogeneous freezing could have occurred due to the depletion of available mineral dust particles in the supersaturated layer. However, back-trajectories suggest that the maximum continuous large-scale shifts of the supersaturated layer were insufficient for this to happen.

Large-scale forcing (w_{LS}) also influences N_i indirectly. When w_{LS} increases, the activation of mineral dust becomes more efficient, and the S_i suppression weakens because ice crystals have less time to consume water vapor, resulting in higher N_i within a relatively short time frame. Conversely, in cases of slower updrafts, the activation process is more gradual, leading to lower overall N_i .

300

305

310

Examining the AGED cases (lower panels in Fig. 9), initially, only a few ice crystals are produced due to the low number of ice-nucleation-active mineral dust particles. The suppression of S_i by these few heterogeneous ice crystals is insufficient, leading to homogeneous freezing. The occurrence of homogeneous freezing is evident from the steep gradient of N_i , as it occurs only when the critical S_i for homogeneous freezing is reached, producing a large number of ice crystals simultaneously. Interestingly, homogeneous freezing occurred at two distinct altitude ranges: between 10.5–11.8 km and within a narrow layer around 12 km. This is evident from the sharp gradient in N_i shown in Fig. 9. Near the top of the cirrus cloud (around 12.5 km), homogeneous freezing is facilitated by the fact that heterogeneous ice crystals deplete less water vapor, leaving more available humidity compared to the lower layers, where larger ice crystals have grown and consumed more moisture. In the 10.5–11.8 km range, sufficient amplitude fluctuations in S_i can occasionally push supersaturation beyond the threshold required for homogeneous freezing, even in the presence of heterogeneous ice. This phenomenon is discussed further in Section 5.1.1.

A notable pattern emerges from the model simulations, as shown in Fig. 10a, where mineral dust particles are depleted in both

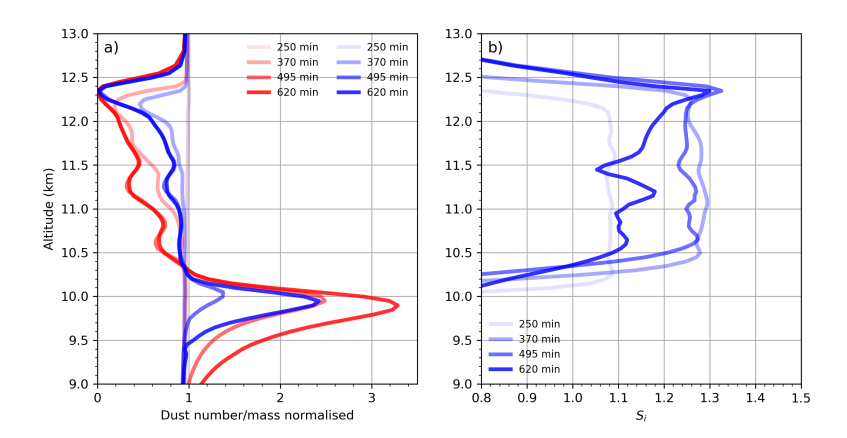


Figure 10. Time series of (a) the mineral dust number/mass (blue/red solid lines respectively) concentration and (b) ice saturation profiles from the beginning to the end of the simulation using the in a STND setuprun. The mineral dust data is presented as normalized dust number/mass, expressed as a fraction of the initial values.

number and mass due to heterogeneous ice nucleation. The most efficient removal of dust occurs between 12 and 12.5 km,

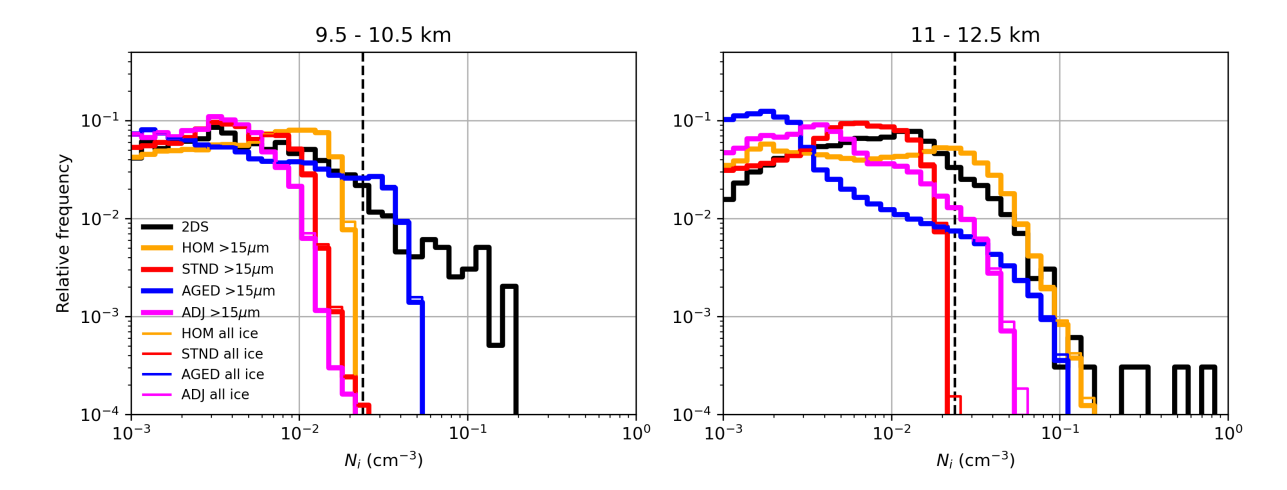


Figure 11. Distribution of N_i in two altitudes that the WB-57F measured continuous statistical data. The measurement data is from 2DS instrument which is in solid black lines. The STND and AGED runs stand for standard with measured mineral dust concentration, AGED for mineral dust particles that have aged. ADJ stands for adjusted profile set up runs and HOM for homogeneous freezing only runs. PALMS-FCAS measured mineral dust concentration shown with black dashed vertical line at 2.05×10^{-2} cm⁻³.

where only a small fraction of dust particles remains by the end of the simulation. Below 12 km, a significant difference is observed between the depletion of dust number concentration and mass concentration, with mass being more heavily depleted. This discrepancy is largely attributed to the preferential activation of larger INPs, which possess greater surface areas and more active ice-nucleating sites, as described by the Ullrich et al. (2017) parameterization.

320

325

330

In contrast, the total number of dust particles remains relatively unaffected compared to the total mass, as the activated particles are predominantly larger dust particles. While these larger particles are less numerous, they play a critical role in ice nucleation under the temperature ranges considered in this study. Between 12 and 12.5 km, the activation of mineral dust particles appears to be less dependent on particle size, as temperatures are below 215 K. For the Ullrich et al. (2017) parameterization, the efficiency difference between particle sizes becomes more pronounced in the temperature range of 215–230 K.

The Figure 10a additionally shows that the activated mineral dust particles eventually sediment to altitudes below saturation over ice (Fig. 10b). As a consequence of cirrus formation, mineral dust particles and other INPs involved can be transported vertically significant distances.

These findings have important implications for interpreting the mineral dust concentration measured by PALMS-FCAS. The clear-air concentration and size distribution of mineral dust may reflect a state influenced by previous nucleation events that occurred before the measurements. Most of the dust measurements were taken at constant altitudes of 10 and 11.2 km, and are not necessarily representative of ice initiation, which for these clouds is at above 12 km as evident from Fig. 10a. While there may be a lack of larger dust particles at these altitudes, their contribution to the overall number concentration would be minimal, and thus not easily detectable.

Additionally, ice crystal vapor growth plays a crucial role in controlling the vertical distribution of humidity as shown in right

panel of Fig. 10b. As ice crystals grow and sediment through the supersaturated layer, they deplete the surrounding humidity. Consequently, the vertical distribution of S_i exhibit a distinct pattern: near the top of cirrus clouds, S_i remains significantly above saturation, while below, it approaches saturation. This occurs because the descending ice crystals progressively consume water vapor during sedimentation.

Figure 11 presents the distribution of N_i at two different altitude levels based on 2DS measurements and model outputs (both for ice crystals filtered above 15 μ m and for all sizes). In the analysis, the modeled N_i and the measured N_i can be directly compared, as the difference between the total modelled N_i and the filtered values for ice crystals above 15 μ m is minimal.

In the STND runs, the maximum N_i did not exceed the mineral dust concentration, indicating that a substantial presence of mineral dust throughout the supersaturated layer effectively suppressed homogeneous freezing. Similar findings were reported by Spichtinger and Gierens (2009), who simulated ice nucleation under varying concentrations of heterogeneous INPs and found that heterogeneous nucleation dominated at INP concentrations above 20 L⁻¹, which is comparable to the measured mineral dust concentration in this study.

In contrast, the AGED runs demonstrated that N_i frequently exceeded the PALMS-measured mineral dust concentration. In the lower cirrus layers, N_i in the AGED runs was significantly higher than in STND, as homogeneous freezing produced high N_i throughout the supersaturated layer. However, at upper altitudes, a significant fraction of N_i remained concentrated around 10^{-3} cm⁻³, suggesting that most of the ice crystal population at these levels originated from heterogeneous nucleation. At lower altitudes, homogeneous freezing occurred more frequently in the AGED case. This increase in homogeneous freezing can be attributed to high-frequency gravity waves, which generated rapid fluctuations in temperature and supersaturation, periodically pushing S_i above the homogeneous freezing threshold. These small-scale perturbations played a crucial role in enhancing ice nucleation activity in the lower cirrus layers.

4.2 The effects of atmospheric fluctuations

340

345

350

355

360

365

The 3D simulations provided a detailed representation of atmospheric variability under the given meteorological conditions. Although the atmosphere within the supersaturated layer remained relatively stable and free from convection, small-scale wave structures resembling gravity waves developed within the model domain. These fluctuations in vertical velocity (w) (Fig. 12a) were primarily driven by vertical wind shear between altitudes of 10 and 12 km. The resulting wave activity caused noticeable variability in S_i , with fluctuations of approximately 0–2% throughout the supersaturated layer during the spin-up phase (at 4 hour mark in Fig. 12b). As the simulations progressed, the amplitude of w fluctuations increased, leading to larger variations in S_i and influencing the intensity of homogeneous freezing present in AGED runs.

To evaluate whether the observed gravity wave-like fluctuations were an artifact of the model domain configuration, a series of sensitivity tests were conducted by varying the horizontal resolution and the domain size in both the X and Y directions. These wave features persisted even in simulations with significantly larger domains, ruling out the possibility that they were predominantly standing waves amplified over time due to insufficient kinetic energy dispersion (Fig. S1). Adjusting the horizontal grid resolution revealed that while the scale of these waves changed slightly, increasing the grid spacing beyond $\Delta x = 100 \text{ m}$

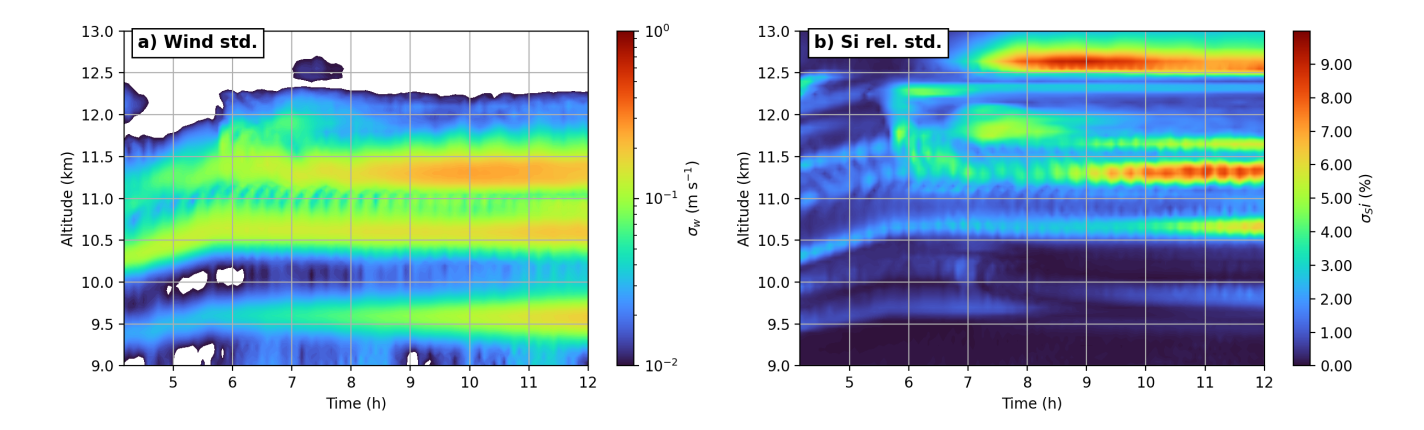


Figure 12. (a) Standard deviation of vertical wind and (b) relative standard deviation of supersaturation over ice S_i shown as shading inside a model domain at cirrus forming altitudes. The velocity fluctuations are generally the same for every set up of simulations used in this study. The variability for S_i was higher at the end of the model runs due to the ice nucleation and subsequent vapor growth of ice crystals affecting the distribution of S_i inside the model domain.

notably reduced the presence of small-scale wave activity.

370

375

380

385

Figure 7 compares the simulated vertical wind velocity (w) with the MMS measurements filtered using a 20-second window. The resulting distributions show a strong resemblance, both exhibiting an ogival-shaped profile similar to that reported by Gierens et al. (2007). This similarity indicates that the model successfully captures vertical wind fluctuations at scales comparable to those observed in the real atmosphere. While the choice of ice nucleation mechanism in the model does introduce some differences between individual runs, the overall shape of the w distribution remains largely unaffected.

The close agreement between the modeled and observed w distributions suggests that the simulated variability effectively mimics the wave activity occurring in the atmosphere. When the MMS w data is filtered using a 150-second window (Fig. 7), the distribution broadens slightly due to the inclusion of mesoscale wave motions with longer wavelengths—features that cannot fully develop within the 3×3 km model domain. Nevertheless, the range of MMS-observed w still aligns well with the modeled w, which is critical since the efficiency of homogeneous freezing is highly sensitive to vertical velocity magnitudes. To further assess the impact of vertical velocity fluctuations on the N_i distribution shown in Fig. 11, reference simulations were performed using a single-column setup, in which horizontal variability and wave activity are absent. As shown in Supplementary Fig. S9, these runs lack the high- N_i tail observed in the 3D simulations, and the frequency of large N_i values is significantly reduced. These findings support the conclusion that gravity waves play a crucial role in shaping cirrus cloud microstructure, consistent with previous studies (Spichtinger and Gierens, 2009; Jensen et al., 2010; Kärcher et al., 2023). The STND distribution, on the other hand, did not experience the influence from the fluctuations, mainly due to heterogeneous freezing being limited more by the relatively small concentration of INPs.

4.3 Accounting for prior cirrus formation

390

395

400

The previous simulations suggested that prior nucleation events likely removed a significant fraction of ice-nucleation-active mineral dust and other INPs from the supersaturated layer (Fig. 10a). To further investigate this effect, additional simulations (ADJ runs) were performed using adjusted dust and humidity profiles designed to approximate post-nucleation conditions (Fig. 10). The S_i profile was modified to reflect humidity depletion caused by earlier freezing events, leading to a peak S_i near the top of the supersaturated layer and lower S_i at lower altitudes.

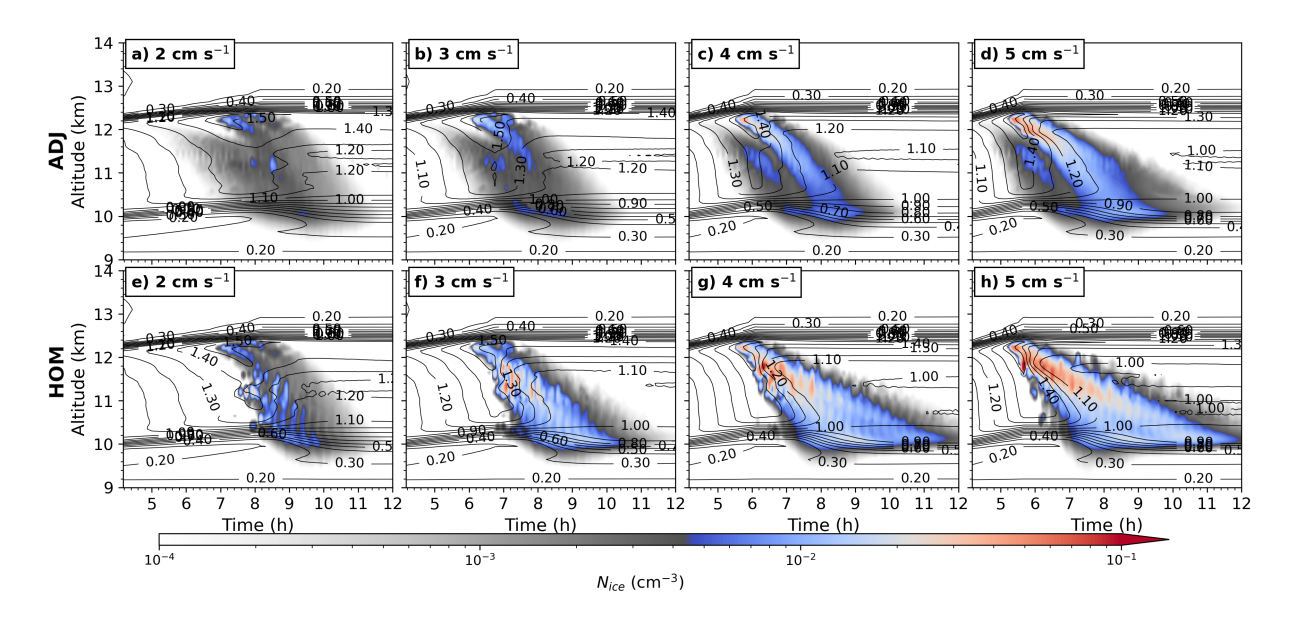


Figure 13. Cirrus clouds produced with $w_{LS} = 2 - 5$ cm s⁻¹ with adjusted mineral dust concentration and humidity ADJ (a-d) and only homogeneous freezing switched on HOM (e-h). The explanation of the details on the figure, see Fig.9.

Direct validation of these elevated S_i values using WB-57F measurements was not possible due to limited sampling; the aircraft only passed through the upper cirrus layers twice, leaving no continuous dataset. Similarly, validating the adjusted dust profiles was challenging because PALMS-FCAS measurements were taken at altitudes where mineral dust activation was less efficient compared to even higher levels. Additionally, data near the top of the cirrus was unavailable, similar to the humidity measurements. Despite these limitations, GOES-16 imagery (Fig. 2) and ERA5 back-trajectory (Fig. 4) suggest that the air mass had undergone intense ice nucleation events before reaching the measurement site. This supports the hypothesis that active dust particles were transported downward below the supersaturated layer, accompanying sedimenting ice crystals. Furthermore, no evidence was found for significant horizontal mixing that could have reintroduced ice-nucleation-active dust particles into the supersaturated region.

Figure 13 presents the simulated cirrus clouds generated using the adjusted setup. Similar to the AGED runs, the cirrus undergoes two distinct nucleation events. The first occurs in the upper cloud layers, where only a small number of ice crystals form (represented by grey shades in Fig. 13, upper panels). This is followed by a second, more intense nucleation event where

homogeneous freezing produces a large number of ice crystals simultaneously.

420

430

435

- To further explore the impact of prior heterogeneous nucleation, additional runs were conducted with heterogeneous freezing turned off (HOM; Fig. 13, right panels). These simulations serve as a reference case where the majority of ice-nucleation-active mineral dust had already been depleted during previous nucleation events when S_i exceeded the threshold for efficient heterogeneous ice nucleation. It was assumed that the remaining mineral dust population was fully activated, corresponding to a frozen fraction of 100%.
- In the HOM runs, homogeneous freezing occurred at all tested values of w_{LS} (Fig. 13, lower panels). In the absence of heterogeneous ice crystals to suppress S_i prior to nucleation, the resulting N_i was the highest among all modeled scenarios. The large number of homogeneously nucleated ice crystals rapidly depleted the available water vapor, enabling the cirrus cloud to reach equilibrium conditions more quickly compared to the ADJ runs. Additionally, clear correlation is evident between N_i and w_{LS} , with the highest N_i observed in the case of $w_{LS} = 5$ cm s⁻¹. This reflects the known sensitivity of homogeneous freezing to the magnitude of vertical velocity, and also the weakening of homogeneous nucleation events due to prior heterogeneous ice nucleation (Spichtinger and Cziczo, 2010).

Returning to the discussion in Sect. 4.2, homogeneous freezing in both the ADJ and HOM runs—similarly to the AGED runs—was influenced by increased N_i within the cirrus. The high-end tail of the N_i distribution in the ADJ and HOM simulations was extended in a manner comparable to that in the AGED cases. Notably, wave-induced fluctuations within the cirrus modulated the rate of homogeneous freezing between 10 and 12 km, where w fluctuations were most pronounced. In contrast, fluctuations were notably weaker between 12 and 12.5 km, where homogeneous freezing was almost entirely dependent on the imposed $w_{\rm LS}$. Consequently, the N_i values in both the ADJ and HOM runs could have been higher if stronger vertical wind fluctuations had been present in the 12–12.5 km layer. Figure 13 supports this by showing that N_i was larger in the altitude regions where vertical velocity variability was greater.

425 4.4 Simulated ice crystal concentration suggests homogeneous freezing limited by initial heterogeneous ice nucleation

In the ADJ runs, the N_i exceeds the mineral dust concentration, particularly in the upper parts of the cirrus cloud between 11 and 12.5 km altitudes (Fig. 11). This is primarily due to the low abundance of mineral dust at these altitudes, which allows supersaturation to rise and enables homogeneous freezing to occur. In contrast, a notable absence of high N_i is observed in the 9.5–10.5 km range in the ADJ runs compared to AGED. This difference can be attributed to the initially lower S_i in the adjusted humidity profile and a higher presence of mineral dust particles, both of which suppress homogeneous freezing in the lower cirrus layers.

Figure 11 also shows the distribution of N_i from homogeneous freezing. The shape of this distribution aligns reasonably well with the 2DS measurements, particularly at the higher end of the N_i spectrum.

Among all the presented simulations, the HOM runs exhibit the closest statistical agreement with the 2DS measurements. This suggests that in the absence of heterogeneous nucleation, homogeneous freezing can generate N_i values that most effectively exceed the background concentration of mineral dust. In the 9.5–10.5 km range, the AGED simulation matches the observed N_i distribution most closely. This agreement is primarily due to the initially high and uniform S_i profile and the relatively low

abundance of heterogeneous ice-nucleating particles in that case. However, considering the evolution of humidity distributing after multiple nucleation events, a uniformly high S_i profile at the start of the model runs is likely an unlikely representation of real atmospheric conditions at the time of measurements. Such profiles would typically require vertically differential cooling rates (which was not evident in this case study from Fig. 4) and very small N_i that would not remove ice supersaturation.

5 Possible limitations of this study

440

445

460

465

In this study, only mineral dust particles were considered as INPs. However, other aerosol components, such as soot, glassy particles, and coated soluble droplets, may also contribute to the heterogeneous INP population and influence the overall ice nucleation activity in cirrus clouds. The ice nucleation efficiency of these additional INP types remains less well understood, and their inclusion in the model would introduce further uncertainties. Furthermore, the conclusions drawn from this study are constrained by the limited sample size of the measured aerosol particles and the restricted vertical sampling, which was conducted only between 10 and 11.2 km. As a result, this study cannot fully validate the simulation outcomes or confirm the robustness of its conclusions.

Furthermore, this study simulated cirrus cloud formation under specific conditions that allowed homogeneous freezing to occur in scenarios where the effects of heterogeneous ice nucleation were limited. If the model had been run under conditions unfavourable to homogeneous freezing, the results would have looked significantly different, with N_i primarily constrained by the number of heterogeneous INPs. While simulating cirrus with lower N_i might have increased the variability of cloud conditions, cirrus clouds with higher N_i would still have dominated the analysis, meaning the overall conclusions would not have been significantly affected.

In contrast, adjusting the initial humidity or increasing the vertical displacement of the supersaturated layer would have favoured more efficient homogeneous freezing. However, the main interpretation of this study remains unchanged. The behaviour of freezing in cirrus clouds—and the occurrence of homogeneous freezing—was shown to be highly dependent on the presence of heterogeneous INPs. Homogeneous freezing did not occur, regardless of the initial S_i or the magnitude of the vertical displacement, when the number of heterogeneous INPs at the cirrus cloud top matched the concentrations from the PALMS-FCAS observed at lower levels.

6 Conclusions

Based on the observations from the MACPEX campaign, the top layer of cirrus clouds on April 16th, 2011, were predominantly formed through homogeneous freezing, as evidenced by ice residual particle (IRP) analysis. Other days of the MACPEX campaign with similar conditions showed that the heterogeneous ice was dominating the IRP analysis. We investigated the role of heterogeneous ice nucleation with the UCLALES-SALSA model, and the results showed that previous events with heterogeneous ice nucleation increases the likelihood of homogeneous freezing occurring during subsequent ice nucleation events. Simulations with measured mineral dust concentrations (STND) showed an almost complete absence of homogeneous freezing due

to heterogeneous ice preventing supersaturation over ice from reaching the critical threshold level for homogeneous freezing.

This suggests that prior heterogeneous demonstrated that heterogeneous ice nucleation events likely depleted the heterogeneous INPs from certain layers of the cirrus clouds. In addition, ice supersaturation is suppressed below the homogeneous freezing threshold, particularly in the colder upper regionsand, resulting in an almost complete absence of homogeneous ice nucleation. Under dynamic conditions allowing supersaturations to reach the homogeneous freezing threshold, such as in the ADJ scenario, this prior depletion indirectly enabled the conditions necessary for subsequent homogeneous freezing to occuroccurrence of homogeneous freezing in later stages.

substantial variability in temperature and S_i . This wave activity resulted in greater variability in the N_i and the rate of homogeneous freezing compared to a scenario without such waves. Notably, the changes in temperature and S_i were slower for large-scale motions, highlighting the significant role of smaller-scale perturbations in affecting ice nucleation processes. Although clear-air INP measurements were not available at cloud top altitudes, MACPEX dust concentrations typically had little vertical structure throughout the cirrus regime. For the Apr 16 case we assume that dust measured at mid- and low-cloud levels was representative of initial cloud top conditions. This underscores the need for improved measurements of aerosol populations, with high sample rate of INPs in both horizontal and vertical directions in future campaign. This study also demonstrated that high resolution three dimensional LES model studies are able to simulate huge variability of N_i inside cirrus that large scale relatively low resolution models simulating the global impacts of cirrus clouds struggle. The LES approach demonstrated that small scale gravity waves can be simulated without using a separate parameterization to simulate the effects of small scale gravity waves (Jensen et al., 2013a). In future, inclusion of more INPs to simulate cirrus clouds could clear

480

485

uncertainties that were not explored in this study.

Finally, vertical shear instabilities within the supersaturated layer led to turbulence and gravity waves, which in turn caused

490 *Code availability.* The source code of the model UCLALES-SALSA is available from GitHub at https://github.com/UCLALES-SALSA/UCLALES-SALSA under release tag MACPEX_icenucl.

Data availability. The campaign data from the MACPEX field study, which was used in this study, is publicly available at the following URL: https://espoarchive.nasa.gov/archive/browse/macpex/WB57. UCLALES-SALSA model data for runs with single seed used for analysis archived at Zenodo (DOI:10.5281/zenodo.14500482. For whole dataset, contact the corresponding author.

Author contributions. KJ made the simulations, analysed the simulation results and wrote major parts of the text. CW contributed to experiment design, size distribution analysis, and provided input on the manuscript. KF provided detailed analysis of PALMS spectra, derived measured concentrations of aerosol components and guided with MACPEX campaign data. JD provided information on interpreting MMS instrument data and analysis of vertical wind data. AL supervised the project and provided input on the manuscript.

Competing interests. Some authors are members of the editorial board of Atmospheric Chemistry and Physics.

Acknowledgements. This work was supported by the Academy of Finland Flagship ACCC (grant no. 337552) and MEDICEN project (grant no. 345125 and 359892). Supercomputing resources were provided by CSC–IT Center for Science, Ltd., Finland. We thank J.C. Wilson for use of the FCAS aerosol data.

References

510

- Ahola, J., Korhonen, H., Tonttila, J., Romakkaniemi, S., Kokkola, H., and Raatikainen, T.: Modelling mixed-phase clouds with the large-eddy model UCLALES–SALSA, Atmospheric Chemistry and Physics, 20, 11 639–11 654, https://doi.org/10.5194/acp-20-11639-2020, 2020.
 - Baum, B. A., Heymsfield, A. J., Yang, P., and Bedka, S. T.: Bulk Scattering Properties for the Remote Sensing of Ice Clouds. Part I: Microphysical Data and Models, Journal of Applied Meteorology, 44, 1885 1895, https://doi.org/10.1175/JAM2308.1, 2005.
 - Baumgartner, M., Rolf, C., Grooß, J.-U., Schneider, J., Schorr, T., Möhler, O., Spichtinger, P., and Krämer, M.: New investigations on homogeneous ice nucleation: the effects of water activity and water saturation formulations, Atmospheric Chemistry and Physics, 22, 65–91, https://doi.org/10.5194/acp-22-65-2022, 2022.
 - Beer, E., Righi, M., Hendricks, J., and Tost, H.: Impacts of ice-nucleating particles on cirrus clouds and radiation derived from global model simulations with MADE3 in EMAC, Atmospheric Chemistry and Physics, 24, 3217–3245, https://doi.org/10.5194/acp-24-3217-2024, 2024.
- Boucher, O., Randall, D., Artaxo, P., Bretherton, C., Feingold, G., Forster, P., Kerminen, V.-M., Kondo, Y., Liao, H., Lohmann, U., Rasch, P.,

 Satheesh, S. K., Sherwood, S., Stevens, B., and Zhang, X. Y.: Clouds and aerosols, pp. 571–657, Cambridge University Press, Cambridge,
 UK, https://doi.org/10.1017/CBO9781107415324.016, 2013.
 - Bryan, G. H., Wyngaard, J. C., and Fritsch, J. M.: Resolution Requirements for the Simulation of Deep Moist Convection, Monthly Weather Review, 131, 2394 2416, https://doi.org/https://doi.org/10.1175/1520-0493(2003)131<2394:RRFTSO>2.0.CO;2, 2003.
- Burrows, S. M., McCluskey, C. S., Cornwell, G., Steinke, I., Zhang, K., Zhao, B., Zawadowicz, M., Raman, A., Kulkarni, G., China, S.,
 Zelenyuk, A., and DeMott, P. J.: Ice-Nucleating Particles That Impact Clouds and Climate: Observational and Modeling Research Needs,
 Reviews of Geophysics, 60, e2021RG000745, https://doi.org/https://doi.org/10.1029/2021RG000745, 2022.
 - Chernoff, D. I. and Bertram, A. K.: Effects of sulfate coatings on the ice nucleation properties of a biological ice nucleus and several types of minerals, Journal of Geophysical Research: Atmospheres, 115, https://doi.org/10.1029/2010JD014254, 2010.
 - Cziczo, D. J. and Froyd, K. D.: Sampling the composition of cirrus ice residuals, Atmospheric Research, 142, 15–31, https://doi.org/https://doi.org/10.1016/j.atmosres.2013.06.012, the 16th International Conference on Clouds and Precipitation, 2014.
 - Cziczo, D. J., Froyd, K. D., Gallavardin, S. J., Moehler, O., Benz, S., Saathoff, H., and Murphy, D. M.: Deactivation of ice nuclei due to atmospherically relevant surface coatings, Environmental Research Letters, 4, 044 013, https://doi.org/10.1088/1748-9326/4/4/044013, 2009.
- Cziczo, D. J., Froyd, K. D., Hoose, C., Jensen, E. J., Diao, M., Zondlo, M. A., Smith, J. B., Twohy, C. H., and Murphy, D. M.: Clarifying the Dominant Sources and Mechanisms of Cirrus Cloud Formation, Science, 340, 1320–1324, https://doi.org/10.1126/science.1234145, 2013.
 - Davis, S., Hallar, A., Avallone, L., and Engblom, W.: Measurement of Total Water with a Tunable Diode Laser Hygrometer: Inlet Analysis, Calibration Procedure, and Ice Water Content Determination, Journal of Atmospheric and Oceanic Technology, 24, 463–475, https://doi.org/10.1175/JTECH1975.1, 2007.
- DeMott, P. J., Prenni, A. J., Liu, X., Kreidenweis, S. M., Petters, M. D., Twohy, C. H., Richardson, M. S., Eidhammer, T., and Rogers, D. C.: Predicting global atmospheric ice nuclei distributions and their impacts on climate, Proceedings of the National Academy of Sciences, 107, 11 217–11 222, https://doi.org/10.1073/pnas.0910818107, 2010.

- Eastwood, M. L., Cremel, S., Wheeler, M., Murray, B. J., Girard, E., and Bertram, A. K.: Effects of sulfuric acid and ammonium sulfate coatings on the ice nucleation properties of kaolinite particles, Geophysical Research Letters, 36, https://doi.org/https://doi.org/10.1029/2008GL035997, 2009.
 - Forster, P., Storelvmo, T., Armour, K., Collins, W., Dufresne, J.-L., Frame, D., Lunt, D., Mauritsen, T., Palmer, M., Watanabe, M., Wild, M., and Zhang, H.: The Earth's Energy Budget, Climate Feedbacks, and Climate Sensitivity, p. 923–1054, Cambridge University Press, Cambridge, United Kingdom and New York, NY, USA, https://doi.org/10.1017/9781009157896.009, 2021.
- Froyd, K., Yu, P., Schill, G., Brock, C., Kupc, A., Williamson, C., Jensen, E., Ray, E., Rosenlof, K., Bian, H., Darmenov, A., Colarco, P.,
 Diskin, G., Bui, T., and Murphy, D.: Dominant role of mineral dust in cirrus cloud formation revealed by global-scale measurements,
 Nature Geoscience, 15, 1–7, https://doi.org/10.1038/s41561-022-00901-w, 2022.
 - Froyd, K. D., Murphy, D. M., Brock, C. A., Campuzano-Jost, P., Dibb, J. E., Jimenez, J.-L., Kupc, A., Middlebrook, A. M., Schill, G. P., Thornhill, K. L., Williamson, C. J., Wilson, J. C., and Ziemba, L. D.: A new method to quantify mineral dust and other aerosol species from aircraft platforms using single-particle mass spectrometry, Atmospheric Measurement Techniques, 12, 6209–6239, https://doi.org/10.5194/amt-12-6209-2019, 2019.
 - Gierens, K., Kohlhepp, R., Dotzek, N., and Smit, H. G.: Instantaneous fluctuations of temperature and moisture in the upper troposphere and tropopause region. Part 1: Probability densities and their variability, Meteorologische Zeitschrift, 16, 221–231, https://doi.org/10.1127/0941?2948/2007/0197, 2007.
- Hersbach, H., B. B. B. P. B. G. H. A. M. S. J. N. J. P. C. R. R. R. I. S. D. S. A. S. C. D. D. T. J.-N.: ERA5 hourly data on pressure levels from 1940 to present. Copernicus Climate Change Service (C3S) Climate Data Store (CDS), https://doi.org/10.24381/cds.bd0915c6, 2023.
 - Jacobson, M. Z.: Fundamentals of Atmospheric Modeling, Cambridge University Press, 2 edn., 2005.

- Jensen, E. J., Toon, O. B., Tabazadeh, A., Sachse, G. W., Anderson, B. E., Chan, K. R., Twohy, C. W., Gandrud, B., Aulenbach, S. M., Heymsfield, A., Hallett, J., and Gary, B.: Ice nucleation processes in upper tropospheric wave-clouds observed during SUCCESS, Geophysical Research Letters, 25, 1363–1366, https://doi.org/https://doi.org/10.1029/98GL00299, 1998.
- Jensen, E. J., Pfister, L., Bui, T.-P., Lawson, P., and Baumgardner, D.: Ice nucleation and cloud microphysical properties in tropical tropopause layer cirrus, Atmospheric Chemistry and Physics, 10, 1369–1384, https://doi.org/10.5194/acp-10-1369-2010, 2010.
 - Jensen, E. J., Diskin, G., Lawson, R. P., Lance, S., Bui, T. P., Hlavka, D., McGill, M., Pfister, L., Toon, O. B., and Gao, R.: Ice nucleation and dehydration in the Tropical Tropopause Layer, Proceedings of the National Academy of Sciences, 110, 2041–2046, https://doi.org/10.1073/pnas.1217104110, 2013a.
- Jensen, E. J., Lawson, R. P., Bergman, J. W., Pfister, L., Bui, T. P., and Schmitt, C. G.: Physical processes controlling ice concentrations in synoptically forced, midlatitude cirrus, Journal of Geophysical Research: Atmospheres, 118, 5348–5360, https://doi.org/https://doi.org/10.1002/jgrd.50421, 2013b.
 - Jensen, E. J., Pfister, L., Jordan, D. E., Bui, T. V., Ueyama, R., Singh, H. B., Thornberry, T. D., Rollins, A. W., Gao, R.-S., Fahey, D. W., Rosenlof, K. H., Elkins, J. W., Diskin, G. S., DiGangi, J. P., Lawson, R. P., Woods, S., Atlas, E. L., Rodriguez, M. A. N., Wofsy, S. C.,
- Pittman, J., Bardeen, C. G., Toon, O. B., Kindel, B. C., Newman, P. A., McGill, M. J., Hlavka, D. L., Lait, L. R., Schoeberl, M. R., Bergman, J. W., Selkirk, H. B., Alexander, M. J., Kim, J.-E., Lim, B. H., Stutz, J., and Pfeilsticker, K.: The NASA Airborne Tropical Tropopause Experiment: High-Altitude Aircraft Measurements in the Tropical Western Pacific, Bulletin of the American Meteorological Society, 98, 129 143, https://doi.org/10.1175/BAMS-D-14-00263.1, 2017.
- Jonsson, H., Wilson, J., Brock, C., Knollenberg, R., Newton, T., Dye, J., Baumgardner, D., Borrmann, S., Ferry, G., Pueschel, R., Woods, D. C., and Pitts, M. C.: Performance of a Focused Cavity Aerosol Spectrometer for Measurements in the Strato-

- sphere of Particle Size in the 0.06-2.0microm-Diameter Range, Journal of Atmospheric and Oceanic Technology, 12, 115–129, https://doi.org/10.1175/1520-0426(1995)012<0115:POAFCA>2.0.CO;2, 1995.
- Joos, H., Spichtinger, P., Lohmann, U., Gayet, J.-F., and Minikin, A.: Orographic cirrus in the global climate model ECHAM5, Journal of Geophysical Research: Atmospheres, 113, https://doi.org/https://doi.org/10.1029/2007JD009605, 2008.
- Joos, H., Spichtinger, P., and Lohmann, U.: Orographic cirrus in a future climate, Atmospheric Chemistry and Physics, 9, 7825–7845, https://doi.org/10.5194/acp-9-7825-2009, 2009.
 - Kanji, Z. A., DeMott, P. J., Möhler, O., and Abbatt, J. P. D.: Results from the University of Toronto continuous flow diffusion chamber at ICIS 2007: instrument intercomparison and ice onsets for different aerosol types, Atmospheric Chemistry and Physics, 11, 31–41, https://doi.org/10.5194/acp-11-31-2011, 2011.
- 585 Kanji, Z. A., Ladino, L. A., Wex, H., Boose, Y., Burkert-Kohn, M., Cziczo, D. J., and Krämer, M.: Overview of Ice Nucleating Particles, Meteorological Monographs, 58, 1.1 1.33, https://doi.org/10.1175/AMSMONOGRAPHS-D-16-0006.1, 2017.
 - Khvorostyanov, V. I. and Curry, J. A.: A new theory of heterogeneous ice nucleation for application in cloud and climate models, Geophysical Research Letters, 27, 4081–4084, https://doi.org/https://doi.org/10.1029/1999GL011211, 2000.
- Kojima, T., Buseck, P., Iwasaka, Y., Matsuki, A., and Trochkine, D.: Sulfate-coated dust particles in the free troposphere over Japan, Atmospheric Research, 82, 698–708, https://doi.org/10.1016/j.atmosres.2006.02.024, 2006.
 - Kokkola, H., Korhonen, H., Lehtinen, K. E. J., Makkonen, R., Asmi, A., Järvenoja, S., Anttila, T., Partanen, A.-I., Kulmala, M., Järvinen, H., Laaksonen, A., and Kerminen, V.-M.: SALSA ndash; a Sectional Aerosol module for Large Scale Applications, Atmospheric Chemistry and Physics, 8, 2469–2483, https://doi.org/10.5194/acp-8-2469-2008, 2008.
- Kokkola, H., Kühn, T., Laakso, A., Bergman, T., Lehtinen, K. E. J., Mielonen, T., Arola, A., Stadtler, S., Korhonen, H., Ferrachat, S.,
 Lohmann, U., Neubauer, D., Tegen, I., Siegenthaler-Le Drian, C., Schultz, M. G., Bey, I., Stier, P., Daskalakis, N., Heald, C. L., and Romakkaniemi, S.: SALSA2.0: The sectional aerosol module of the aerosol–chemistry–climate model ECHAM6.3.0-HAM2.3-MOZ1.0, Geoscientific Model Development, 11, 3833–3863, https://doi.org/10.5194/gmd-11-3833-2018, 2018.
 - Koop, T., Luo, B., Tsias, A., and Peter, T.: Water Activity as the determinant for homogeneous ice nucleation in aqueous solutions, Nature, 406, 611–4, https://doi.org/10.1038/35020537, 2000.
- Krämer, M., Rolf, C., Luebke, A., Afchine, A., Spelten, N., Costa, A., Meyer, J., Zöger, M., Smith, J., Herman, R. L., Buchholz, B., Ebert, V., Baumgardner, D., Borrmann, S., Klingebiel, M., and Avallone, L.: A microphysics guide to cirrus clouds Part 1: Cirrus types, Atmospheric Chemistry and Physics, 16, 3463–3483, https://doi.org/10.5194/acp-16-3463-2016, 2016.

- Krämer, M., Rolf, C., Luebke, A., Afchine, A., Spelten, N., Costa, A., Meyer, J., Zöger, M., Smith, J., Herman, R. L., Buchholz, B., Ebert, V., Baumgardner, D., Borrmann, S., Klingebiel, M., and Avallone, L.: A microphysics guide to cirrus clouds Part 1: Cirrus types, Atmospheric Chemistry and Physics, 16, 3463–3483, https://doi.org/10.5194/acp-16-3463-2016, 2016.
- Krämer, Rolf, C., Spelten, N., Afchine, A., Fahey, D., Jensen, E., Khaykin, S., M., Kuhn, T., Lawson, P., Lykov, A., Pan, L. L., Riese, M., Rollins, A., Stroh, F., Thornberry, T., Wolf, V., S., P., Quaas, J., and Sourdeval, O.: A microphysics guide Spichtinger, to cirrus Climatologies of clouds and humidity from observations, Atmospheric Chemistry and Physics, 20, 12569-12608, https://doi.org/10.5194/acp-20-12569-2020, 2020.
- Kärcher, B. and Lohmann, U.: A parameterization of cirrus cloud formation: Homogeneous freezing of supercooled aerosols, Journal of Geophysical Research: Atmospheres, 107, AAC 4–1–AAC 4–10, https://doi.org/https://doi.org/10.1029/2001JD000470, 2002.

- Kärcher, B., Jensen, E. J., and Lohmann, U.: The Impact of Mesoscale Gravity Waves on Homogeneous Ice Nucleation in Cirrus Clouds, Geophysical Research Letters, 46, 5556–5565, https://doi.org/l0.1029/2019GL082437, 2019.
- Kärcher, B., DeMott, P. J., Jensen, E. J., and Harrington, J. Y.: Studies on the Competition Between Homogeneous and Heterogeneous Ice Nucleation in Cirrus Formation, Journal of Geophysical Research: Atmospheres, 127, e2021JD035805, https://doi.org/https://doi.org/10.1029/2021JD035805, 2022.

625

- Kärcher, B., Jensen, E. J., Pokrifka, G. F., and Harrington, J. Y.: Ice Supersaturation Variability in Cirrus Clouds: Role of Vertical Wind Speeds and Deposition Coefficients, Journal of Geophysical Research: Atmospheres, 128, e2023JD039324, https://doi.org/10.1029/2023JD039324.e2023JD039324.2023JD039324.2023.
- Lawson, R. P.: Effects of ice particles shattering on the 2D-S probe, Atmospheric Measurement Techniques, 4, 1361–1381, https://doi.org/10.5194/amt-4-1361-2011, 2011.
- Lawson, R. P., O'Connor, D., Zmarzly, P., Weaver, K., Baker, B., Mo, Q., and Jonsson, H.: The 2D-S (Stereo) Probe: Design and Preliminary Tests of a New Airborne, High-Speed, High-Resolution Particle Imaging Probe, Journal of Atmospheric and Oceanic Technology, 23, 1462 1477, https://doi.org/10.1175/JTECH1927.1, 2006.
- Liu, X., Shi, X.and Zhang, K. J. E. J., Gettelman, A., Barahona, D., Nenes, A., and Lawson, P.: Sensitivity studies of dust ice nuclei effect on cirrus clouds with the Community Atmosphere Model CAM5, Atmospheric Chemistry and Physics, 12, 12 061–12 079, https://doi.org/10.5194/acp-12-12061-2012, 2012.
- Ngo, D., Diao, M., Patnaude, R. J., Woods, S., and Diskin, G.: Aerosol–cloud interactions in cirrus clouds based on global-scale airborne observations and machine learning models, Atmospheric Chemistry and Physics, 25, 7007–7036, https://doi.org/10.5194/acp-25-7007-2025, 2025.
 - Pan, L., Bowman, K., Atlas, E., Wofsy, S., Zhang, F., Bresch, J., Ridley, B., Pittman, J., Homeyer, C., Romashkin, P., and Cooper, W.: The stratosphere-troposphere analyses of regional transport 2008 experiment, Bulletin of the American Meteorological Society, 91, 327–342, https://doi.org/10.1175/2009BAMS2865.1, 2010.
- Pan, L. L., Atlas, E. L., Salawitch, R. J., Honomichl, S. B., Bresch, J. F., Randel, W. J., Apel, E. C., Hornbrook, R. S., Weinheimer, A. J., Anderson, D. C., Andrews, S. J., Baidar, S., Beaton, S. P., Campos, T. L., Carpenter, L. J., Chen, D., Dix, B., Donets, V., Hall, S. R., Hanisco, T. F., Homeyer, C. R., Huey, L. G., Jensen, J. B., Kaser, L., Kinnison, D. E., Koenig, T. K., Lamarque, J.-F., Liu, C., Luo, J., Luo, Z. J., Montzka, D. D., Nicely, J. M., Pierce, R. B., Riemer, D. D., Robinson, T., Romashkin, P., Saiz-Lopez, A., Schauffler, S., Shieh, O., Stell, M. H., Ullmann, K., Vaughan, G., Volkamer, R., and Wolfe, G.: The Convective Transport of Active Species in the
 Tropics (CONTRAST) Experiment, Bulletin of the American Meteorological Society, 98, 106 128, https://doi.org/10.1175/BAMS-D-14-00272.1, 2017.
 - Pruppacher, H. R. and Klett, J. D.: Microphysics of Clouds and Precipitation, Atmospheric and Oceanographic Sciences Library, 18, https://doi.org/10.1007/978-0-306-48100-0, 1997.
- Reid, J. S., Koppmann, R., Eck, T. F., and Eleuterio, D. P.: A review of biomass burning emissions part II: intensive physical properties of biomass burning particles, Atmospheric Chemistry and Physics, 5, 799–825, https://doi.org/10.5194/acp-5-799-2005, 2005.
 - Ren, C. and Mackenzie, A. R.: Cirrus parametrization and the role of ice nuclei, Quarterly Journal of the Royal Meteorological Society, 131, 1585–1605, https://doi.org/10.1256/qj.04.126, 2005.
 - Rolf, C., Krämer, M., Schiller, C., Hildebrandt, M., and Riese, M.: Lidar observation and model simulation of a volcanic-ash-induced cirrus cloud during the Eyjafjallajökull eruption, Atmospheric Chemistry and Physics, 12, 10 281–10 294, https://doi.org/10.5194/acp-12-10281-2012, 2012.

- Sassen, K. and Benson, S.: Ice nucleation in cirrus clouds: A model study of the homogeneous and heterogeneous modes, Geophysical Research Letters, 27, 521–524, https://doi.org/https://doi.org/10.1029/1999GL010883, 2000.
- Schneider, J., Höhler, K., Wagner, R., Saathoff, H., Schnaiter, M., Schorr, T., Steinke, I., Benz, S., Baumgartner, M., Rolf, C., Krämer, M., Leisner, T., and Möhler, O.: High homogeneous freezing onsets of sulfuric acid aerosol at cirrus temperatures, Atmospheric Chemistry and Physics, 21, 14 403–14 425, https://doi.org/10.5194/acp-21-14403-2021, 2021.

- Scott, S. G., Bui, T. P., Chan, K. R., and Bowen, S. W.: The Meteorological Measurement System on the NASA ER-2 Aircraft, Journal of Atmospheric and Oceanic Technology, 7, 525 540, https://doi.org/https://doi.org/10.1175/1520-0426(1990)007<0525:TMMSOT>2.0.CO;2, 1990.
- Seifert, A. and Siewert, C.: An ML-Based P3-Like Multimodal Two-Moment Ice Microphysics in the ICON Model, Journal of Advances in Modeling Earth Systems, 16, e2023MS004206, https://doi.org/https://doi.org/10.1029/2023MS004206, e2023MS004206 2023MS004206, 2024.
 - Smith, R. B.: The Influence of Mountains on the Atmosphere, vol. 21 of *Advances in Geophysics*, pp. 87–230, Elsevier, https://doi.org/https://doi.org/10.1016/S0065-2687(08)60262-9, 1979.
- Spichtinger, P. and Cziczo, D. J.: Impact of heterogeneous ice nuclei on homogeneous freezing events in cirrus clouds, Journal of Geophysical

 Research: Atmospheres, 115, https://doi.org/10.1029/2009JD012168, 2010.
 - Spichtinger, P. and Gierens, K.: Modelling of cirrus clouds Part 2: Competition of different nucleation mechanisms, Atmospheric Chemistry and Physics, 9, 2319–2334, https://doi.org/10.5194/acpd-8-9061-2008, 2009.
 - Stevens, B., Moeng, C.-H., and Sullivan, P. P.: Large-Eddy Simulations of Radiatively Driven Convection: Sensitivities to the Representation of Small Scales, Journal of the Atmospheric Sciences, 56, 3963 3984, https://doi.org/https://doi.org/10.1175/1520-0469(1999)056<3963:LESORD>2.0.CO:2, 1999.
 - Stevens, B., Moeng, C.-H., Ackerman, A. S., Bretherton, C. S., Chlond, A., de Roode, S., Edwards, J., Golaz, J.-C., Jiang, H., Khairoutdinov, M., Kirkpatrick, M. P., Lewellen, D. C., Lock, A., Müller, F., Stevens, D. E., Whelan, E., and Zhu, P.: Evaluation of Large-Eddy Simulations via Observations of Nocturnal Marine Stratocumulus, Monthly Weather Review, 133, 1443 1462, https://doi.org/10.1175/MWR2930.1, 2005.
- Sullivan, R. C., Petters, M. D., DeMott, P. J., Kreidenweis, S. M., Wex, H., Niedermeier, D., Hartmann, S., Clauss, T., Stratmann, F., Reitz, P., Schneider, J., and Sierau, B.: Irreversible loss of ice nucleation active sites in mineral dust particles caused by sulphuric acid condensation, Atmospheric Chemistry and Physics, 10, 11 471–11 487, https://doi.org/10.5194/acp-10-11471-2010, 2010.
 - Sölch, I. and Kärcher, B.: A large-eddy model for cirrus clouds with explicit aerosol and ice microphysics and Lagrangian ice particle tracking, Quarterly Journal of the Royal Meteorological Society, 136, 2074–2093, https://doi.org/https://doi.org/10.1002/qi.689, 2010.
- Thomson, D. S., Schein, M. E., and Murphy, D. M.: Particle Analysis by Laser Mass Spectrometry WB-57F Instrument Overview, Aerosol Science and Technology, 33, 153–169, https://doi.org/10.1080/027868200410903, 2000.
 - Tonttila, J., Maalick, Z., Raatikainen, T., Kokkola, H., Kühn, T., and Romakkaniemi, S.: UCLALES-SALSA v1.0: a large-eddy model with interactive sectional microphysics for aerosol, clouds and precipitation, Geoscientific Model Development, 10, 169–188, https://doi.org/10.5194/gmd-10-169-2017, 2017.
- Tully, C., Neubauer, D., Omanovic, N., and Lohmann, U.: Cirrus cloud thinning using a more physically based ice microphysics scheme in the ECHAM-HAM general circulation model, Atmospheric Chemistry and Physics, 22, 11 455–11 484, https://doi.org/10.5194/acp-22-11455-2022, 2022.

- Twohy: Measurements of Saharan Dust in Convective Clouds over the Tropical Eastern Atlantic Ocean, Journal of the Atmospheric Sciences, 72, 75–81, https://doi.org/https://doi.org/10.1175/JAS-D-14-0133.1, 2014.
- 690 Ullrich, R., Hoose, C., Möhler, O., Niemand, M., Wagner, R., Höhler, K., Hiranuma, N., Saathoff, H., and Leisner, T.: A New Ice Nucleation Active Site Parameterization for Desert Dust and Soot, Journal of the Atmospheric Sciences, 74, 699 717, https://doi.org/10.1175/JAS-D-16-0074.1, 2017.
 - Wendisch, M., Pöschl, U., Andreae, M. O., Machado, L. A. T., Albrecht, R., Schlager, H., Rosenfeld, D., Martin, S. T., Abdelmonem, A., Afchine, A., Araùjo, A. C., Artaxo, P., Aufmhoff, H., Barbosa, H. M. J., Borrmann, S., Braga, R., Buchholz, B., Cecchini, M. A., Costa, A., Curtius, J., Dollner, M., Dorf, M., Dreiling, V., Ebert, V., Ehrlich, A., Ewald, F., Fisch, G., Fix, A., Frank, F., Fütterer, D., Heckl,
- A., Curtius, J., Dollner, M., Dorf, M., Dreiling, V., Ebert, V., Ehrlich, A., Ewald, F., Fisch, G., Fix, A., Frank, F., Fütterer, D., Heckl, C., Heidelberg, F., Hüneke, T., Jäkel, E., Järvinen, E., Jurkat, T., Kanter, S., Kästner, U., Kenntner, M., Kesselmeier, J., Klimach, T., Knecht, M., Kohl, R., Kölling, T., Krämer, M., Krüger, M., Krisna, T. C., Lavric, J. V., Longo, K., Mahnke, C., Manzi, A. O., Mayer, B., Mertes, S., Minikin, A., Molleker, S., Münch, S., Nillius, B., Pfeilsticker, K., Pöhlker, C., Roiger, A., Rose, D., Rosenow, D., Sauer, D., Schnaiter, M., Schneider, J., Schulz, C., de Souza, R. A. F., Spanu, A., Stock, P., Vila, D., Voigt, C., Walser, A., Walter, D., Weigel, R.,
- Weinzierl, B., Werner, F., Yamasoe, M. A., Ziereis, H., Zinner, T., and Zöger, M.: ACRIDICON–CHUVA Campaign: Studying Tropical Deep Convective Clouds and Precipitation over Amazonia Using the New German Research Aircraft HALO, Bulletin of the American Meteorological Society, 97, 1885 1908, https://doi.org/10.1175/BAMS-D-14-00255.1, 2016.
- Zängl, G., Reinert, D., Rípodas, P., and Baldauf, M.: The ICON (ICOsahedral Non-hydrostatic) modelling framework of DWD and MPI-M: Description of the non-hydrostatic dynamical core, Quarterly Journal of the Royal Meteorological Society, 141, 563–579, https://doi.org/https://doi.org/10.1002/qj.2378, 2015.